https://doi.org/10.1016/j.cej.2020.125516

Title page

Mini-Review of Perovskite Oxides as Oxygen Electrocatalysts for Rechargeable Zinc–Air Batteries

Yawen Dai,[1] Jie Yu,[1,*] Chun Cheng,[1] Peng Tan,[2] Meng Ni[1,*]

[1] Department of Building and Real Estate, The Hong Kong Polytechnic University, Hung Hom, Kowloon, Hong Kong, China

[2] Department of Thermal Science and Energy Engineering, University of Science and Technology of China, Hefei 230026, Anhui, China

[*]Corresponding authors

E-mail addresses: yujie19920114@njtech.edu.cn (Jie Yu), meng.ni@polyu.edu.hk (Meng Ni)

Abstract

Zn–air batteries (ZABs) have been considered to be promising candidates for the next generation of energy storage devices. The sluggish kinetics of the oxygen reduction and oxygen evolution reactions (ORR and OER, respectively) at the air cathode are the key obstacles that limit the power output and energy efficiency of ZABs, and thus, it is important to develop bifunctional electrocatalysts that present high activity for both the ORR and OER, long durability, and low cost. Perovskite oxides hold great potential for fabricating air cathodes owing to their high intrinsic electrocatalytic activity, facile synthesis, and great compositional and structural flexibility. Herein, we briefly overview the development of perovskite oxides for ZAB applications. The fundamentals of ZABs and OER/ORR pathways of perovskite oxides are introduced. Strategies for activity tuning are also provided, followed by the mechanistic explanation and experimental methods of catalyst fabrication. Moreover, ZAB performance examples are also listed for convenient comparison. Lastly, remaining challenges and possible future directions of perovskite oxide-based air cathodes are discussed.

Keywords: Zn–air battery; perovskite oxide; electrocatalysis; oxygen evolution; oxygen reduction

1. Introduction

Given the growing energy demands of the modern society, it is urgent to exploit advanced energy conversion and storage techniques. As a clean and efficient type of energy, electricity is favored for its end-use energy consumption in both industry and people's daily life.[1] Rechargeable batteries have been developing fast in the past decades and have been used to provide electricity for various applications, such as mobile phones and electric vehicles (EV).[2] Li–ion batteries (LIBs) are mature devices that dominate the rechargeable battery market.[3] However, the insufficient energy density of LIBs (theoretical value ~400 Wh kg^{-1}) is a significant drawback that has been associated with the need for frequent recharging and limited mileage of EVs.[4,5] Moreover, the flammable electrolytes and relatively expensive Li used for LIBs also hinder their large-scale applications.[1,6] Therefore, exploring new generations of rechargeable batteries is desirable.

Recently, rechargeable Zn–air batteries (ZABs) have become increasingly attractive owing to their high theoretical energy density of 1350 Wh kg^{-1}, safe aqueous electrolytes, low cost, and environmental friendliness.[1,7] However, the practical application of rechargeable ZABs is still impeded by the sluggish kinetics of the oxygen reduction reaction (ORR) and oxygen evolution reaction (OER) at the air cathode during the discharge and charge processes, respectively, which result in their low energy efficiencies (lower than 65%).[1] Noble metals and their compounds, such as Pt for ORR, and IrO_2/RuO_2 for OER, are currently the best electrocatalysts; however, they are always active for one reaction and inert for the reverse one.[8,9] Moreover, their high

cost and low stability hinder their widespread use.[1] Hence, developing noble metal-free electrocatalysts with high activity for both the ORR and OER is significant for high-performance ZABs.

Perovskite oxides have been regarded as promising efficient bifunctional electrocatalyst candidates due to their high intrinsic activity, compositional flexibility, and easy synthesis which is feasible for large-scale production. The typical formula of perovskite oxides is ABO_3 and their structure is cubic, as illustrated in Figure 1a, where the larger-size rare-earth or alkali metal cations occupy the 12-fold O-coordinated A-sites, and the smaller-size transition metal cations occupy the 6-fold O-coordinated B-sites.[10] Approximately 90% of the elements in the periodic table could substitute the A- or B-sites of perovskite oxides.[11] Moreover, the perovskite structure allows a large range of O nonstoichiometry.[12] In addition to the typical perovskite structure, the perovskite family includes derivatives, such as double, quadruple, and layered perovskites. The above-mentioned characteristics confer perovskite oxides their great compositional and structural flexibility, which enables the use of diverse strategies to manipulate their electronic structure toward high electrocatalytic activity.[12] Previous reviews focused on nanostructured perovskite oxides and perovskite/carbon composites; however a specific review of the applications of perovskite oxides for ZABs has never been published.[10,12] Herein, we focus on perovskite oxides as bifunctional oxygen electrocatalysts and overview their applications for ZABs. This review includes the mechanisms of the OER and ORR on perovskite oxides, activity tailoring strategies and corresponding experimental methods, and the performance of ZABs featuring

perovskites oxides. Lastly, the current challenges and suggestions for the future development of perovskite oxide-based air cathodes are also presented.

2. Fundamental Reactions in ZABs

Rechargeable ZABs can be generally classified into conventional liquid batteries and flexible solid-state batteries.[1] A typical liquid ZAB (Figure 1b) consists of a Zn anode, a concentrated alkaline electrolyte, and an air cathode.[13] The air cathode for the OER and ORR is considered to be the most critical component that determines the battery performance. The air cathode presents multilayer structure that consists of electrocatalysts, a gas diffusion layer, and a current collector. The hydrophilicity/hydrophobicity balance is significant for the interfacial structure of air cathodes. The hydrophilic side supports the bifunctional electrocatalysts and provides access to the electrolyte, and the hydrophobic side provides microchannels for the diffusion of gases toward the catalytic sites and barriers that prevent the leakage of the electrolyte.[3] In addition, flexible solid-state ZABs have been attracting the interest of researchers owing to the increase in the development of various flexible electronics.[14-16] The representative configuration of a flexible ZAB is illustrated in Figure 1c, where the solid state electrolyte, which is always an alkaline gel, is sandwiched between the Zn anode and air cathode, and flexible current collectors are attached to both electrodes.[5]

The discharge and charge processes of ZABs (forward and backward arrows, respectively) are based on the following electrochemical reactions:[3]

Anode: $$Zn + 4OH^- \rightleftarrows Zn(OH)_4^{2-} + 2e^-, \qquad E = -1.26\ V\ vs.SHE \qquad (1)$$

Cathode: $O_2 + 2H_2O + 4e^- \rightleftarrows 4OH^-, \quad E = 0.4\,V\ vs.SHE$ (2)

Overall: $2Zn + O_2 \rightleftarrows 2ZnO, \quad E = 1.66\,V$ (3)

Despite the theoretical voltage of 1.66 V, the reported ZABs have always exhibited charge voltages that exceeded 2 V and discharge voltages lower than 1.2 V.[3] Due to the multielectron transfer coupled with proton transfer process, both OER and ORR suffer from sluggish intrinsic kinetics. Moreover, for the ORR reaction, the competition between the desired $4e^-$ pathway and the unfavored $2e^-$ pathway also adds to the difficulty of achieving high activity.[17] Therefore, the large gap between the theoretical discharge voltage of ZAB and the practical value mainly originates from the overpotential of the OER and ORR at the air cathode, which highlights the significance of developing active bifunctional oxygen electrocatalysts.

A deep understanding on the OER and ORR mechanisms is prerequisite for the rational design of active catalysts. For perovskite oxides and other transition metal-based oxides, ORR catalysis is believed to proceed along the pathway illustrated in Figure 1d. Namely, ORR catalysis starts from the creation of B-OH^- species on the metal oxide surface, which is accompanied by the reduction of the B metal cation for charge-compensation. The B-OH^- species interact with the absorbed O_2 and deliver electrons through the variable valence states of the B metal cation.[10,18,19] Two possible mechanisms have been proposed for the OER on perovskite oxides, namely the absorbate evolution and lattice O participated mechanisms (AEM and LOM, respectively).[20] For the AEM, the B-site transition metal is considered to be the active site, and the OER takes place along the reverse pathway of the ORR presented in Figure

1d.[10] The LOM describes the OER catalysis on perovskite oxides based on the exchange of lattice O species (Figure 1f).[21,22] The LOM highlights the key role of surface O vacancies, which could modulate the ionic diffusion rate and electronic structure of perovskite oxides.[10] Additionally, numerous studies have been carried out to identify an appropriate descriptor that could reveal the structure-activity relationship of perovskite oxides. The OER and ORR activities of perovskite oxides greatly depends on their electronic structure, such as the B-site metal-oxygen covalency, d electron number of the B-site cations, and position of the O 2p band center relative to the Fermi level.[10,23] Considering the fact that electrocatalysis reactions occur at the electrocatalyst-electrolyte-gas interface, the surface properties of electrocatalysts should be a critical concern when constructing the structure-activity relationship. A lot of reports on perovskite oxides indicate that the surface of transition-metal oxides favors electron localization over the bulk itinerant electron state.[24,25] Furthermore, Shao-Horn et al. demonstrated that the primary descriptor for OER and ORR activity of perovskite oxides is the extend of e_g orbital filling of the surface B-site transition metals. [18,26] Volcano-shape quantitative correlations between the e_g filling and intrinsic OER/ORR activity of perovskite oxides were discovered, which indicated the highest activity in alkaline solutions with near-unity occupancy of e_g orbital.[18,26] Under the guidance of the above mechanistic studies, great advances have been achieved in developing highly active bifunctional electrocatalysts and perovskite oxide-based air cathodes.

3. Recent Advances in Perovskites Oxides as Oxygen Electrocatalysts for ZABs

3.1. Phase Tailoring

To date, most perovskites reported as oxygen electrocatalysts for ZABs are single perovskites with the general formula ABO_3, such as $Ba_{0.5}Sr_{0.5}Co_{0.8}Fe_{0.2}O_3$, $La_{0.8}Sr_{0.2}MnO_3$, $CaMn_{0.75}Nb_{0.25}O_3$, $LaNiO_3$, and $LaMn_{0.9}Co_{0.1}O_3$.[27-32] More specifically, $Ba_{0.5}Sr_{0.5}Co_{0.8}Fe_{0.2}O_3$ is one of the pioneering bifunctional electrocatalysts toward both the OER and ORR under alkaline conditions, and its catalytic activity is comparable to that of Pt/C.[27] Therefore, $Ba_{0.5}Sr_{0.5}Co_{0.8}Fe_{0.2}O_3$ might be a promising cathode material for rechargeable ZABs. Among a series of La-based perovskite oxides, $LaMO_3$ (M = Cr, Mn, Fe, Co, Ni), $LaMnO_3$ and $LaCoO_3$ demonstrated the highest activity for the ORR and OER, respectively.[28] Vignesh *et al.* successfully fabricated Ni-doped $LaCo_{0.96}O_{3-\delta}$ (denoted as $La(Co_{0.71}Ni_{0.25})_{0.96}O_{3-\delta}$) porous nanotubes using an advanced electrospinning method.[33] The synergistic effect of Ni and Co and remarkable porous nanotube micro/nano-structure rendered $La(Co_{0.71}Ni_{0.25})_{0.96}O_{3-\delta}$ bifunctionally active for the OER and ORR at the oxygen electrode of rechargeable ZABs. At the current density of 5 A g^{-1}, the potential gaps for the 1st and 20th cycle of the ZAB featuring $La(Co_{0.71}Ni_{0.25})_{0.96}O_{3-\delta}$ were 0.529 and 0.792 V, respectively, which were significantly smaller than those of $LaCo_{0.97}O_{3-\delta}$ and state-of-the-art Pt/C materials.

Several other perovskites, such as double and quadruple perovskites ($A_2BB'O_6$ and $AA'_3B_4O_{12}$, respectively), have been demonstrated to exhibit better oxygen catalytic

behavior than simple single perovskites.[34-37] Yamada *et al.* employed a solid-state reaction method to synthesize a quadruple manganese perovskite oxide, AMn_7O_{12} (A = Ca, La), as efficient OER and ORR catalyst.[34] Such structural transformation led to the OER and ORR activities of AMn_7O_{12} (A = Ca, La) being higher than those of simple single manganese perovskites ($AMnO_3$ (A = Ca, La)). Using density functional theory (DFT) calculations, the authors concluded that the structural features rather than the bulk electronic states of quadruple perovskites (Figures 2a and b), are responsible for their high catalytic performance. The O–O bond was likely to be directly formed between two O-related species adsorbed on the A′- and B-site Mn cations, and thus it facilitated the OER. This finding emphasized the great potential of AMn_7O_{12} perovskites for ZABs. In another work from Kirsanova *et a*l., the quadruple $YBaCo_4O_{7.3}$ was also reported to be an efficient bifunctional OER/ORR electrocatalyst. The decent OER activity was due to the overstoichiometric oxygen that induced octahedral Co positions as active sites, while the excellent ORR activity was attributed to the tetrahedral-coordinated Co with a compact coordination environment which optimized the binding energy of the absorbates.[38] In addition, the layered crystal architecture of the $PrBa_{0.85}Ca_{0.15}MnFeO_{5+\delta}$ cation-ordered double perovskite endowed it with ordered O vacancy channels and numerous surface O defects, which facilitated the subsequent bifunctional oxygen electrocatalysis.[35] Here, such bifunctionality is better than the state-of-the-art $Ba_{0.5}Sr_{0.5}Co_{0.8}Fe_{0.2}O_3$ perovskite oxides. Recently, Kim *et al.* investigated the bifunctional oxygen electrocatalytic properties of $PrBa_{0.5}Sr_{0.5}Co_{2-x}Ni_xO_{5+\delta}$ with different Ni contents (x = 0, 0.1, 0.2 and 0.3, which are

named as PBSCN0, PBSCN-1, PBSCN-2, PBSCN-3, respectively) for ZABs.[36] It was determined that by taking advantage of the abundant surface O species and synergy of the various Co chemical states (Co^{2+}, Co^{3+}, Co^{4+}), the $PrBa_{0.5}Sr_{0.5}Co_{1.9}Ni_{0.1}O_{5+\delta}$ sample exhibited better ORR and OER activities (including more favorable onset potentials and larger limiting currents) than other perovskite samples (Figures 2c and d). Accordingly, the ZABs featuring $PrBa_{0.5}Sr_{0.5}Co_{1.9}Ni_{0.1}O_{5+\delta}$ achieved smaller charge–discharge voltage gaps and remarkable cyclic durability, as illustrated in Figures 2e and f.[36]

3.2. Defect Engineering

Defect engineering is of great significance for various electrocatalytic processes. The presence of abundant defects in metal oxides could strongly affect their charge distribution, spin transition, and band structure. As the most common type of defect in perovskite oxides, O vacancies are always induced to promote electrocatalytic activity. The methods used to create O vacancies include treatment with reductive agents or gases, and fabricating A-site excessive or A-site deficient perovskite oxides.

Ou *et al.* used Li metal as the reductive agent to capture O from perovskite oxides. $La_{0.6}Sr_{0.4}Co_{0.2}Fe_{0.8}O_{3-\delta}$ with surface disordered layer was fabricated via Li reduction (Figure 3a). The density of O vacancies could be tuned by adjusting the amount of Li, and thus the balance between the chemical stability and O exchange kinetics could be achieved. The optimized $La_{0.6}Sr_{0.4}Co_{0.2}Fe_{0.8}O_{3-\delta}$ exhibited good bifunctional catalytic activity, and its OER and ORR potentials were 1.66 and 0.70 V vs. RHE (potential versus reversible hydrogen electrode), respectively, at 10 mA cm^{-2}.[39] In addition, by

treating the perovskite oxides under inert/reducing atmosphere, their concentration of O vacancies could be easily controlled, and therefore, the electronic structure of the catalysts could be tuned.[29,40,41] O deficiency-rich $LaMn_{0.75}Co_{0.25}O_{3-\delta}$ nanofibers (LMCO-2) were produced from regular $LaMn_{0.75}Co_{0.25}O_{3-\delta}$ samples (LMCO) via a two-step calcination method under H_2/Ar and Ar atmosphere.[40] Such treatment method maximized the number of O vacancies and led to the creation of high oxidation states of the transition metal. This contributed to the excellent OER activity of LMCO-2 and the 27.5-fold higher current density of LMCO-2 compared with that of the LMCO catalyst at the overpotential of 450 mV. The ZAB featuring LMCO-2 as the air electrode catalyst presented the large power density of 35 mW cm^{-2} and robust 70 h cycling ability. Besides, Cho *et al.* reported that as the complex $Ba_{0.5}Sr_{0.5}Co_xFe_{1-x}O_{3-\delta}$ perovskites (x = 0.2 and 0.8, denoted as BSCF5528 and BSCF5582, respectively) were heat-treated at 950 °C under Ar atmosphere (BSCF5528-Ar and BSCF5582-Ar, respectively), their local structure, which included numerous O vacancies was possibly changed from the ideal $Pm\bar{3}m$ phase to a highly O-deficient brownmillerite *Pcmn* phase. Moreover, the amorphous layer on the surface of BSCF5582 showed a significant 10-fold increase while a little change was observed for this BSCF5528 sample, as depicted in Figure 4a.[41] Consequently, both the OER and ORR electrocatalytic performances of BSCF5582-Ar in 0.1 M KOH were significantly lower than those of BSCF5582. Conversely, the ORR activity of BSCF5528-Ar in 0.1 M KOH was significantly higher than that of BSCF5528 (Figures 4b and c). Such trends were closely correlated to the surface structure and defect chemistry of the samples (Figures

4d-i). Compared with BSCF5582-Ar, the more symmetric atomic configuration around the Co sublattice in BSCF5528-Ar brought about higher crystallinity and less structural stress, which was more insensitive to heat treatment and more structurally stable. In addition, many O vacancies ($V_o^{\cdot\cdot}$), especially Co–$V_o^{\cdot\cdot}$, which were regarded as the main catalytic active centers, could be accommodated in the symmetric Co sublattice of BSCF5528-Ar, and hence favored its electrocatalytic performance. Such results indicate the significant potential applications of BSCF perovskites for ZABs.

Moreover, A-site excess could facilitate the formation of O vacancies.[42] Xu *et al.* synthesized $(La_{0.8}Sr_{0.2})_{1+x}MnO_3$ as efficient bifunctional oxygen electrocatalyst. As presented in Figure 3b, B-site Mn and O deficiencies were induced to accommodate the excessive number of A-site La/Sr cations. The authors inferred that the oxygen vacancy formation might be due to the loss of manganite, but the detailed mechanism still demands further investigation. The O_2^{2-}/O^- species occupied the O vacancies, and thus O_2 absorption was enhanced and the ORR was accelerated. Simultaneously, the positively charged O vacancies could attract OH^- ions to benefit the OER.[43] Additionally, the introduction of A-site deficiencies could well tune the valence states of the B-site cations and induce more O vacancies, and thus, could alter the surface electronic structure and states.[44] Consequently, the oxygen catalytic activity on the air electrode of ZABs could be regulated. The oxygen vacancies in A-site deficient perovskite oxides were studied more thoroughly than those in A-site excessive cases. As illustrated in Figure 3c, the $V_o^{\cdot\cdot}$ formation mechanism can be explained by the electro-neutrality principle. The deficiency of A-site cations would decrease the

positive charge in lattice, and thus promote the formation of $V_o^{\cdot\cdot}$ and increase of B-site cation valence state for charge compensation.[44,45] Recently, different degrees of A-site deficiencies were induced in $La_{0.8}Sr_{0.2}MnO_3$-based perovskite ($(La_{0.8}Sr_{0.2})_{1-x}MnO_3$ (x = 0, 0.02, 0.05), which were denoted as LSM1, LSM2, and LSM3, respectively) by adjusting the mole ratio of the metal precursors during the sol–gel synthesis process; in addition, the B-site Mn cations of LSM3 were partially replaced by Fe, and the obtained perovskite was denoted as LSMF.[46] With increasing A-site deficiencies, a lattice reduction was observed from the red shift of the main peak in the enlarged X-ray diffraction (XRD) pattern (Figure 3d), which was due to more generation of smaller Mn cations (Mn^{4+}), and the overall particle size was decreased. For LMSF, the larger ionic radius of Fe^{4+} relative to that of Mn^{4+} resulted in the blue shift of the main peak and hence the increased lattice. According to the X-ray photoelectron spectroscopy results, the concentration of O vacancies decreased as follows: LSMF > LSM3 > LSM2 > LSM1 (Figure 3e). As the A-site deficiency increased, the content of Mn^{4+} gradually increased from 49.8% to 58.7%. Owing to its numerous O vacancies and proper valence state of Mn, LSM3 presented greatly enhanced OER activity and slightly improved ORR activity under alkaline conditions compared with LSM1. Moreover, the further partial substitution of Mn by Fe in LSM3 led to the catalytic performance of LSFM for the OER and ORR being higher than that of LSM3. When LSMF was used as the cathode catalyst for ZABs, the discharge voltage was approximately 1.19 V, which was slightly lower than that of the benchmark ZAB featuring Pt/C as the catalyst (~1.25 V). However, the continuous use time of LSMF (56 300 s) was significantly longer than

that of Pt/C (53 180 s) during the one-time consumption of the Zn electrode. In addition, at the constant current density of 10 mA cm^{-2}, the discharge–charge performance of LSMF was more stable than that of Pt/C; moreover, LSMF presented a smaller variance in the voltage gap between the 1st and 100th cycle than Pt/C (Figures 3f and g).

In addition to the increase in the concentration of O vacancies of BSCF perovskites to manipulate their catalytic behavior, the introduction of excessive O^{2-} anions into their lattice also plays an important role.[47] The same researchers determined that the heat treatment of BSCF5582 under O_2 flow enabled an approximately 3 nm thin layer with an approximately 3 nm thick intrinsic spinel structure between the external amorphous layer and internal cubic perovskite to be cleared up, and consequently, enhanced the OER and ORR electrocatalytic performances of BSCF5582.[47] However, considering the huge diversity of practical applications, Wu *et al.* observed that when $La_{0.6}Ca_{0.4}CoO_{3-\delta}$ was heat-treated above 300 °C under O_2 flow, both its OER and ORR electrocatalytic performances were reduced.[48]

Beside oxygen vacancies, metal defects can also greatly influence the electrocatalytic activity of perovskite oxides. Zhang *et al.* proposed a p-block metal regulation strategy, where the typical p-metal Sn^{4+} was *in situ* dissolved from the SnNiFe perovskite nanodots to create abundant surface defects. As a result, the lattice oxygen turned into incompact amorphous layer and actuated electron transfer, and the surface transition metals was oxidized to higher chemical states which are more favorable for OER. The activated SnNiFe perovskite exhibited excellent OER activity comparable to IrO_2. [49]

3.3. Cation Doping

Heteroatom doping, which is conducive to the atomic rearrangement, electron density redistribution, and valence state changes of the developed catalysts, has been considered to be a useful method for improving the electrocatalytic activity and stability for the OER and ORR on the cathodes of ZABs. To optimize the oxygen catalytic performance of perovskite oxides, it is important to carefully select dopants and adjust their concentration. To date, the A- and B-sites of the perovskite structure have been considered to be the most used sites for functional doping. For the A-site doping of perovskite oxides, the coexistence of La and Sr has been widely reported to modify the electronic structure and basic properties of perovskite oxides, and thus, to improve their performance.[21,50-53] Azizi *et al.* demonstrated that $Sr_{2-x}La_xFeMoO_6$ adequately doped with La (x = 0.5) featured lower electrical resistivity than other members of the $Sr_{2-x}La_xFeMoO_6$ (x = 0, 0.25, and 1) series, and therefore its OER/ORR electrocatalytic activity was superior to that of the other $Sr_{2-x}La_xFeMoO_6$ perovskite oxides.[52] Jung *et al*. improved the electrocatalytic activity of $La_x(Ba_{0.5}Sr_{0.5})_{1-x}Co_{0.8}Fe_{0.2}O_{3-\delta}$, which is a La-doped BSCF perovskite, in ZABs for both the ORR and OER by simultaneously adjusting the La doping amount and calcination temperature.[53] Figures 5a and b illustrate the growth of perovskite particles and phase changes for $La_x(Ba_{0.5}Sr_{0.5})_{1-x}Co_{0.8}Fe_{0.2}O_{3-\delta}$, where the perovskite particle size noticeably decreased as the calcination temperature decreased and the amount of La dopant increased. Moreover, a pure cubic phase only appeared in the temperature range between the higher and lower critical temperatures. Based on these patterns, the optimized synthesis conditions (La stoichiometry of 0.7 and calcination temperature of 700 °C) favored the

formation of the La-doped BSCF perovskite with very small particles (~50 nm in size), which was denoted as $La_{0.7}$-50 nm. Owing to its small particles, the resultant $La_{0.7}$-50 nm perovskite presented excellent ORR and OER electrochemical activities in 0.1 M KOH alkaline solution. Furthermore, the performance of $La_{0.7}$-50 nm in a ZAB was tested in the presence of a highly concentrated alkaline solution (6 M KOH). As expected, $La_{0.7}$-50 nm presented superior electrochemical activity and charge–discharge recycling stability at the current density of 10.5 mA cm^{-2} compared to 20% Pt/C. The charge–discharge overpotential of $La_{0.7}$-50 nm changed from 0.75 V for the 1st cycle to 1.0 V for the 100th cycle, whereas the overpotential of Pt/C increased from 0.8 to 1.5 V, respectively, as displayed in Figures 5c and d.

The partial substitution of the B-site transition metals of perovskites with other transition metals, such as Fe, Co, Ni, and Mn, has been typically used to control several structural properties that are strongly related to their electrocatalytic performance for both the OER and ORR.[30,36,54-57] According to Hua *et al.*, the introduction of moderate amounts of Fe dopant into $PrBaMn_2O_{5+\delta}$ double perovskites, enabled the B-site cations to achieve high chemical valence and optimal e_g orbital filling, which contributed to obtaining better bifunctional oxygen electrocatalysis.[35] Wang *et al.* reported a series of $La_{0.8}Sr_{0.2}Co_{1-x}Mn_xO_3$ perovskites (x = 0, 0.2, 0.4, 0.6, 0.8, 1) via controlling the concentration of Mn dopant during the sol–gel synthesis.[50] The obtained $La_{0.8}Sr_{0.2}Co_{0.4}Mn_{0.6}O_3$ (LSCM-60) displayed the optimum bifunctional activity under alkaline conditions, and it delivered better performance and cycle durability than the benchmark Pt/C when used as the cathode electrocatalyst for ZAB

(Figure 5e). The excellent activity of LSCM-60 was attributed to the improved O_2 adsorption/desorption capability, as well as the doping-induced regulation of B-site cation chemical valences. The highest Co^{3+}/Co^{2+} ratio in LSCM-60 (Figure 5f) satisfied the near-unity e_g occupation principle.[50] Additionally, Zhu *et al.* demonstrated that doping a small amount of Pd atoms into the B-sites of $LaFeO_3$ conferred the obtained material excellent ORR activity and stability. Such doping induced the formation of stable $Pd^{3/4+}$ species, which were deemed essential for promoting the ORR.[58]

The doping of non-metal elements, particularly P, has been demonstrated to be effective for enhancing the ORR performance of perovskite oxides under alkaline conditions.[59] P-doped $La_{0.8}Sr_{0.2}MnO_{3-\delta}$ (LSMP) was prepared via a sol–gel method using metal nitrates/acetates and $NH_4H_2PO_4$ as the raw materials, and its cubic structure was identical to that of the parent $La_{0.8}Sr_{0.2}MnO_{3-\delta}$ (LSM) perovskite.[59] The formation of LSMP, and in particular the presence of 5 at.% P in its structure, effectively increased the Brunauer–Emmett–Teller surface area and enhanced the O_2 adsorption behavior of LSMP relative to those of LSM, and thus, contributed to the excellent ORR activity of LSMP, which presented the onset potential of 0.93 V vs. RHE and diffusion-limited current density of −5.07 mA cm^{-2}, as well as superior operation durability compared with LSM.

The structural stability of perovskite oxides strongly depends on the stability of the BO_6 octahedral architecture; however, the partial doping of the A- and B-site elements by the other one with a different chemical valence and cation radius might also enhance the structural stability of perovskite oxides in various surrounding

environments, such as at different potential bias, high temperature, high or low pH, and high O_2/H_2 partial pressure.[29,35,57] Hua *et al.* introduced a small amount of Ca cations into the A-sites of $PrBaMnFeO_{5+\delta}$ (PBMF) and successfully stabilized its structure under the operating condition with electrochemical potential. Specifically, the surface decomposition that would generate an amorphous and A-site element-rich shell under a certain potential bias could be efficiently suppressed by the incorporation of Ca into the A-sites.[35] Consequently, the electrocatalytic activity of PBMF, the Ca-free counterpart, toward the OER and ORR was significantly lower than that of the Ca-doped PBMF sample. Lyu *et al.* revealed that the partial incorporation of Nb cations at the B-sites of $CaMnO_{3-\delta}$ (CMO) conferred strong resistance to the structure under reducing atmosphere; moreover, H_2-treated Nb-doped CMO could preserve the orthorhombic (*Pnma*) structure of pristine CMO and Nb-doped CMO.[29] Conversely, after H_2 treatment, CMO underwent phase change from *Pnma* to *Pbam*. However, such variations conferred the CMO perovskite relatively low electrical conductivity and hampered the further adjustment of its e_g orbital occupancy. Consequently, Nb doping and subsequent H_2 treatment synergistically activated the bifunctionality of CMO, and the obtained material presented greatly potential for ZAB applications.

3.4. Morphology Control

When perovskite oxides are conventionally synthesized using the sol–gel and solid state methods, extensive calcination at high temperature is always required to arrange the A- and B-site atoms into homogenous perovskite crystal structures.[60] Consequently, the obtained crystals could be several micrometers in size, which would

lead to very limited surface areas and insufficient active sites for electrocatalytic reactions. In addition, conventionally prepared perovskite oxides lack efficient mass transport channels owing to their pore-free and featureless morphology, and that further hampers their electrocatalytic activity.[12] Therefore, significant efforts have been dedicated to nanostructuring perovskite oxides to exploit their full potential for oxygen catalysis.

The template-assisted method is often used to introduce pores in the structure of perovskite oxides. Templates could be generally categorized into soft and hard. Amphiphilic molecules could be used as soft templates, and they undergo self-assembly in the precursor solutions and guide the precipitation of metal ions.[12] When meso-macroporous $LaMnO_3$, which was synthesized using Pluronic P-123 as the soft template, was used for ZABs, it exhibited the discharge voltage of 1.158 V at 25 mA cm^{-2}.[61] Polyethylenimine was also used as soft template during the synthesis of nanostructured $LaCo_{1-x}Ni_xO_3$. The obtained material possessed porous network morphology and exhibited enhanced OER and ORR activity compared to its bulk counterpart.[3] Soft templates can be easily eliminated, and thus, using them does not allow precise morphology control. In contrast, hard templates are prepatterned solid materials that restrict the precipitation of metal ions to the voids and interspaces of the templates.[62] Hard templates are relatively stable during the growth of products, and thus, the morphology of the obtained products is more controllable and reproducible. Hence, hard templates are more widely used than soft ones. For example, closed-packed polymethyl methacrylate microspheres were used as the hard template to synthesize a

three-dimensional (3D) porous $La_{0.95}Ag_{0.05}FeO_{3-\delta}$ catalyst with ordered pore distribution and well-controlled pore size.[63] In addition, an inorganic salt, namely anhydrous potassium phosphate (K_3PO_4) powder, was demonstrated to be a novel hard template, and was used to synthesize hierarchically porous $PrBa_{0.5}Sr_{0.5}Co_{1.5}$-$Fe_{0.5}O_{5+\delta}$, which presented the high surface area of 148 $m^2\ g^{-1}$.[64] Moreover, mesoporous $La_{0.6}Ca_{0.4}CoO_3$ catalyst with the large surface area of 235 $m^2\ g^{-1}$ was prepared using mesoporous silica as the hard template. The obtained $La_{0.6}Ca_{0.4}CoO_3$ was used as the air electrode of a ZAB, which displayed the discharging and charging voltages of 1.15 and 2.01 V, respectively, at 20 mA cm^{-2}; moreover, these voltages remained constant during a 130 h cycling test.[65]

Another popular method used to maximize the specific surface area of perovskite oxides is the construction of featured morphologies, such as one-dimensional (1D) nanorods, nanofibers, and nanotubes. The main methods used to synthesize such 1D perovskite oxides are the hydrothermal and electrospinning methods. During hydrothermal synthesis, materials are crystallized from a pressurized aqueous solution at high temperature. The hydrothermal method could lower the subsequent annealing temperature by several hundred degrees compared to the sol–gel method, and thus, could limit grain agglomeration and preserve the featured morphology of the synthesized perovskite oxides.[12] $La(Co_{0.55}Mn_{0.45})_{0.99}O_3$ and $LaFe_xNi_{1-x}O_3$ nanorods have been successfully prepared using the hydrothermal method.[66,67] However, the hydrothermal method requires that the A- and B-site ions co-precipitate homogenously and stoichiometrically, which might be difficult to achieve for some metal ions, and

therefore, the use of this method is limited. Electrospinning is an alternative method used to synthesize 1D perovskite oxides. Figure 6a illustrates the typical electrospinning setup. The syringe contains the stoichiometric metal precursor solution mixed with a polymer that assists the fiber formation process. The high-voltage power supplier provides an electric field between the metal needle and conductive collector.[68] Calcination in air is conducted to convert the as-spun fibers into perovskite oxide fibers, and during this step, hollow structures or nanotubes might form owing to the Kirkendall effect.[69,70] Bu *et al.* prepared $PrBa_{0.5}Sr_{0.5}Co_{2-x}Fe_xO_{5+\delta}$ via electrospinning, and obtained nanofibers 300 nm in diameter. The nanofibers consisted of 20-40 nm nanoparticles and 5-10 nm nanopores, and their surface area was eight times higher than that of the bulk counterpart. The $PrBa_{0.5}Sr_{0.5}Co_{2-x}Fe_xO_{5+\delta}$ nanofibers were used to fabricate an air cathode for ZABs, which presented the power density of 127 mW cm^{-2}.[56] Bian *et al.* synthesized Mg-doped $LaNiO_3$ nanofibers and used them as efficient bifunctional catalyst, which exhibited the low ΔE (potential gap between the OER potential at 10 mA cm^{-2} and the ORR half-wave potential, $\Delta E=E_{j=10}-E_{1/2}$) of 0.99 V; moreover its ZAB charge–discharge cycle stability exceeded 110 h at 10 mA cm^{-2}.[71] Peng *et al.* synthesized sulfur-doped $CaMnO_3$ (CMO/S) nanotubes on large scale via electrospinning followed by calcination and sulfurization. The diameter of the nanotubes was uniform (~250 nm) and their length was in the micrometer range. The unique pore-abundant nanotube structure (Figure 6b) significantly facilitated gas and ion diffusion, led to the rapid oxygen transport into and out of the structure, and reduced the overpotentials for the OER and ORR. An aqueous ZAB featuring CMO/S nanotubes

achieved the peak power density of 152 mW cm^{-2}, small charge–discharge voltage gap of 0.67 V, and round-trip energy efficiency of 64.8% at 5 mA cm^{-2} (Figure 6c). Moreover, the flexible all-solid-state ZAB that was assembled using CMO/S nanotubes (Figure 6d, inset), displayed excellent rechargeable performance. The discharge voltage of the flexible ZAB exceeded 1 V at 0.5 mA cm^{-2} when the ZAB was bent at various angles in the range of 0° to 150° (Figure 6d), which indicated its great potential for wearable electronic devices applications.[72]

Beside the common methods described above, some new methods have been recently developed for nanostructuring perovskite oxides to achieve higher electrocatalytic activity. A novel solid-state gelation method was reported for the synthesis of perovskite oxide aerogels.[73] The preparation of perovskite oxide aerogels is challenging owing to the conflict between the mild solvent interactions that occur during conventional aerogel synthesis processes and high temperature required for the formation of perovskite phases. This aspect was addressed by Shao-Horn *et al.* who used carbon as the solvent to mediate the solid-state gelation process. The synthesis method is illustrated in Figure 7a. The $LaMnO_x$ precursor nanoparticles were physically dispersed on the porous carbon support (Figure 7b), and were subsequently subjected to accelerated calcination to stimulate their gelation. The carbon matrix burned during the high temperature calcination step, and that facilitated the fusion and connection of the nanoparticles (Figure 7c) into a 3D gel structure (Figure 7d). The obtained aerogel presented low density, highly continuous porosity, and the large specific surface area of 74.2 m^2 g^{-1}. Moreover, the increase in the valence state of Mn

was observed, and was attributed to the decrease in crystal size. Therefore, the r-$LaMnO_{3\pm\delta}$ aerogel exhibited the remarkable mass activity of 66.2 A g^{-1} at 0.8 V vs. RHE, which is the highest value of all perovskite oxides reported in the literature. Furthermore, this solid-state gelation method was demonstrated to be versatile and allowed the production of a variety of perovskite oxide aerogels, including $LaFeO_3$, $LaNiO_3$, $LaCoO_3$, $La_{0.5}Sr_{0.5}CoO_3$, and $La_{0.5}Sr_{0.5}Co_{0.5}Fe_{0.5}O_3$.[73] In addition, Kuai *et al.* proposed a spray-pyrolysis approach for the synthesis of mesoporous $LaMnO_{3+\delta}$ microspheres.[74] The precursor solution was sprayed using an ultrasonic humidifier to generate mist. Then, the nitrites were subjected to pyrolysis in a tube furnace and the powder was collected using a pumped filter (Figure 7e). The aqueous ZAB assembled using mesoporous $LaMnO_{3+\delta}$ microspheres presented the peak power density of 198.6 mW cm^{-2}, which was comparable to that of the benchmark Pt/C catalyst (Figure 7f).[74]

In addition, self-supporting nanoarray structure also play a significant role in energy related materials. The binder-free characteristic could improve the conductivity of the electrocatalysts and accessibility of active sites, and the nanoarray structure could provide abundant channels for mass and electron transport. The fabrication of self-supporting perovskite oxide nanoarray always relies on the template-assisted method.[75] The porous silicon or alumina membranes are used as templates, which are filled up with polymeric precursors and heated to form perovskite oxides, followed by wet-chemical etching of templates. Self-supporting perovskite oxide nanoarrays have been applied in memory devices, piezoelectric generators, and terahertz generators,[75] however, their application in OER/ORR electrocatalysis and ZABs has

never been reported to the best of our knowledge. Considering the good ZAB performance delivered by self-supporting nanoarray structures such as Co_3O_4 nanowire arrays on stainless-steel and N-doped carbon nanotube arrays on Ni foam,[76] we anticipate that self-supporting perovskite oxide nanoarrays should be promising as air cathodes for ZABs.

3.5. Building Hybrids

Building hybrid composites is a strategy typically used to fabricate highly efficient electrocatalysts. The synergistic effects of different materials in hybrids could lead to the catalytic activity of hybrids exceeding those of the single component counterparts. Building hybrids could improve the intrinsic catalytic activity of perovskite oxides by tailoring their electronic structure.[10] Besides, most perovskite oxides are monofunctional and catalyze only the OER or ORR, whereas bifunctional catalysts could be fabricated by combining separate active sites for the OER and ORR in a hybrid.

Combining the ORR benchmark Pt catalyst with an OER-active perovskite oxide has been recently considered as an attractive method for fabricating affordable bifunctional oxygen electrocatalysts. Cuicci *et al.* synthesized a Pt_3Ni nanoparticle-decorated $La_{0.9}Mn_{0.9}Pt_{0.075}Ni_{0.025}O_{3-\delta}$(LSMPN) catalyst using an in situ exolution method, and the obtained catalyst presented superior OER and ORR activities compared to those of the single component LSMPN.[77] Recently, Shao *et al.* reported the preparation of a high-performance Pt-$Sr(Co_{0.8}Fe_{0.2})_{0.95}P_{0.05}O_{3-\delta}$ (SCFP)/C composite bifunctional oxygen electrocatalyst using a facile ball milling approach.[78] The rapid electron transfer via the Pt–O–Co bonds led to strong electronic interactions

between Pt and SCFP (Figure 8a), which were confirmed by the decrease in the valence state of Co and increase in the valence state of Pt in the composite compared to those in the isolated components. In addition, the higher energy barrier of the ORR and OER could be overcome by the spillover effect between Pt and SCFP (Figure 8a). Consequently, the Pt-SCFP/C composite exhibited higher OER activity than IrO_2 and comparable ORR activity to 20 wt% Pt/C, whereas the cost of Pt-SCFP/C was 1/3 lower than those of 20 wt% Pt/C and IrO_2. An aqueous ZAB based on this composite catalyst displayed the charge–discharge voltage gap of 0.77 V at 5 mA cm^{-2}. This voltage gap slightly increased to 0.86 V after 80 h of cycling testing (Figure 8b), which demonstrated the outstanding activity and durability, and also the great promise of Pt-SCFP/C for practical applications.[78]

Owing to the high cost and scarcity of Pt, precious metal-free materials are highly demanded. Carbon materials are most commonly used for building hybrids with perovskite oxides, owing to their low cost, high conductivity, good ORR activity, and diverse carbon structure. Connecting the low-conductive perovskite with highly conductive carbon scaffolds could accelerate electron transport.[10] In addition, the dispersion of perovskite oxides nanoparticles throughout a high surface area carbon matrix could inhibit particle aggregation, and thus, could increase the number of accessible active sites.[79] Different types of carbon materials, such as carbon nanotubes, graphene and its derivatives, carbon dots, and biomass-derived porous carbon, have been successfully integrated with perovskite oxides. Because most carbon frameworks cannot withstand the high-temperature calcination under O-rich

atmosphere that is required for the crystallization of perovskites, conventional integration could be performed via physical mixing or growing carbon materials on pre-synthesized perovskite oxides.[79,80] These methods are not favorable to the homogenous distribution of the hybrid components, and accordingly, some one-pot synthesis methods have emerged to address this problem. The hydrothermal method was used to synthesize $LaNiO_3$ nanorods supported on reduced graphene oxide, which delivered the low charge–discharge voltage gap of 0.97 V at 25 mA cm^{-2} in an aqueous ZAB.[81] Chen *et al.* proposed a novel rapid gel auto-combustion synthesis method for $La_{0.99}MnO_{3.03}$/C at low temperature.[79] The gel that anchored the metal ions was heated in a tube furnace at 180 °C, and during that step the reactants self-ignited with the assistance of NH_4NO_3 and O_2 as the oxidizers, and organic additives and carbon as the fuels. The heat released during self-combustion was used for the quick nucleation and growth of $La_{0.99}MnO_{3.03}$ into the unburned carbon, which resulted in the formation of homogeneous nanocomposites. The active perovskite centers were well dispersed and were surrounded by highways for electron transportation, which contributed to the high-performance of the aqueous ZAB (peak power density of 430 mW cm^{-2}).[79] In addition to acting as conductive and dispersion supports, as mentioned above, carbon materials could form strongly coupled interfaces with perovskite oxides, which could lead to the redistribution of electrons. Moreover, these carbon materials could modulate the absorption of reactants and intermediate species, and thus, could tune the intrinsic activity of the hybrid catalysts. Lee *et al.* mixed $NdBa_{0.25}Sr_{0.75}Co_2O_{5.9}$ catalyst particles with polypyrrole (Ppy)/carbon, and the obtained material presented reduced

overpotentials for both the OER and ORR.[82] DFT calculations indicated that the distance between the Co ion and O_2 molecules was significantly lower in the presence of Ppy than in its absence, and therefore, it was concluded that Ppy/C facilitated the chemisorption of O_2 on perovskite and accelerated the ORR.[82] Kim *et al.* demonstrated the presence of a synergistic effect between $(PrBa_{0.5}Sr_{0.5})_{0.95}Co_{1.5}Fe_{0.5}O_{5+\delta}$ (PBSCF) and 3D N-doped graphene (3DNG).[70] Compared to pristine PBSCF and 3DNG, the composite presented shorter N–O and Co–O bonds and longer O–O bonds of the absorbed O_2, which indicated that the absorption of O_2 was activated, and that accelerated the ORR (Figure 8c). In addition, owing to the PBSCF-3DNG interaction, the energy gap between the Co/Fe 3d orbital and O 2p band center of PBSCF was reduced (Figure 8d). This implied that the covalency between the B-site metals and surface lattice O increased, which enhanced the OER activity of PBSCF. Therefore, the PBSCF/3DNG composite exhibited excellent bifunctionality in an aqueous ZAB, and delivered the charge–discharge voltage of 0.63 V at 10 mA cm^{-2} after 110 cycles, which was superior to that of the benchmark Pt/C-IrO_2 couple.[70] A similar synergistic effect was observed between $Sm_{0.5}Sr_{0.5}CoO_{3-\delta}$ and 3DNG.[69] Despite the various advantages of carbon materials, carbon corrosion at high oxidative potentials, particularly in alkaline media, continues to hinder the long-term stability of bifunctional catalysts. Using highly graphitized carbon could improve the corrosion resistance of the composites; however, highly graphitized carbon would only slow the corrosion rate rather than completely eradicate

the corrosion of carbon. Therefore, the development of carbonless bifunctional catalysts has been encouraged.[10]

Nonprecious metal-based oxides, hydroxides, and phosphides have been widely explored as partners of perovskite oxides for building hybrid catalyst.[83-85] The hybrid synthesis strategies include infiltration, one-pot synthesis, selective surface etching, and in situ growth of secondary phase. Gui *et al.* prepared the $Gd_{0.1}Ce_{0.9}O_{2-\delta}$ (GDC) decorated $(Pr_{0.5}Ba_{0.5})CoO_{3-\delta}$ (PBC) catalyst using an infiltration technique. The abundant intrinsic O vacancies of GDC could facilitate the absorption of O_2 and H_2O molecules on the hybrid catalyst, and therefore, boosted its OER and ORR activity. The power density of the aqueous ZAB featuring the GDC/PBC catalyst was 207 mW cm^{-2}, and its charge–discharge voltage gap was 0.78 V at 10 mA cm^{-2}.[84] Shao's group reported a $SrCo_{0.8}Fe_{0.2}O_{3-\delta}/Sr_3B_2O_6$ hybrid synthesized by one-pot sol-gel method. The catalytic-inactive $Sr_3B_2O_6$ acted as a proton acceptor that significantly enhanced the OER activity of $SrCo_{0.8}Fe_{0.2}O_{3-\delta}$.[86] In addition, a $La_{0.7}Sr_{0.3}MnO_3$(LSM)-MnO_2 hierarchical core–shell structure was fabricated by partially dissolving the surface A-site ions in HNO_3.[87] The loose and porous MnO_2 nanoparticles wrapped on LSM significantly increased the specific surface area of the structure. Moreover, the Mn–O bonds were tuned to a moderate length towards optimal intrinsic activity for both the OER and ORR, and that led to the high-performance of the aqueous ZAB featuring the LSM-MnO_2 catalyst, which presented the peak power density of 181.4 mW cm^{-2}.[87] Feng *et al.* fabricated $Co_3O_4/La_{0.3}Sr_{0.7}CoO_3$ spinel/perovskite hybrid by selectively etching the surface La on the parent perovskite oxide followed by surface

recrystallization of spinel Co_3O_4 by calcination. This synthesis allowed a strong chemical interaction at the hybrid interface, which activated the lattice oxygen and simultaneously promoted the OER and ORR activity.[88] In addition to enhancing the catalytic activity as in the above-mentioned examples, surface decoration with secondary phases could circumvent the reconstruction of the perovskite oxide surface under oxidative potentials, and thus improve the working lifetime of the electrocatalysts. Majee *et al.* reported that the stability of the NiFe-LDH/$Ba_{0.6}Sr_{0.4}Co_{0.79}Fe_{0.21}O_{2.67}$ (BSCF) composite was significantly higher than that of the bare BSCF.[85] NiFe-LDH was integrated on the surface of BSCF via polyethyleneimine-mediated hydrothermal growth, which promoted the formation of a crystalline boundary between the two components, and thus benefited the transportation of electrons. The charge–discharge cycling curve of the aqueous ZAB featuring the NiFe-LDH/BSCF catalyst indicated that its performance was steady for 100 h at 5 mA cm^{-2}.[85] Moreover, Luo and coworkers decorated CoP nanoparticles on $PrBa_{0.5}Sr_{0.5}Co_{1.5}Fe_{0.5}O_{5+\delta}$ perovskite nanofibers, where the synthesis were carried out through an in situ exsolution followed by phosphatization. The resulted hybrid electrocatalyst delivered decent ZAB performance with a power density of 138 mW cm^{-2} and a voltage gap of 0.84 V at 10 mA cm^{-2}.[83]

3.6. Tuning Lattice Strain

In addition to the conventional strategies introduced before, researchers recently demonstrated that tuning the lattice strain opened a new way to improve the

electrocatalytic activity of metals and metal oxides. The lattice strain may influence the surface absorption energy of reaction intermediates, the surface defect formation energy, or the charge transport property of electrocatalysts.[89,90] Epitaxial deposition is a commonly used method to fabricate strained thin film perovskite oxides, where the strain can be controlled from tensile (+) to compressive (-) by the lattice-mismatch between the substrates and products. Besides, the strain can be relaxed by increasing the film thickness.[91] Shao-Horn's group took $LaCoO_3$ (LCO) perovskite as the study platform to investigate the strain-dependent OER and ORR activity in alkaline solution, finding that the compressively strained (-0.5%) LCO exhibited the lowest bifunctional activity, whereas the moderate tensile strain (1.8%) led to the highest bifunctional activity. The tensile strain-induced activity enhancement was attributed to the deviation of local symmetry, which would decrease the Co-O bond distance and thus increase the strength of absorbed oxygen bond.[91] In addition, Petrie *et al*. studied $LaNiO_3$ (LNO) perovskites with various lattice strains for alkaline oxygen electrocatalysis, and they found controversial conclusion with that from Shao-Horn's group, which indicated that the oxygen electrocatalytic activity was benefited by compressive strain instead of tensile strain.[92] The authors systematically tuned the strains on the (001) LNO perovskite by using various lattice-mismatched substrates, including (001) $LaSrAlO_4$ (LSAO), (001) $LaAlO_3$(LAO), (001) $(LaAlO_3)_{0.3}(SrAl_{0.5}Ta_{0.5}O_3)_{0.7}$ (LSAT), (001) $SrTiO_3$ (STO), and (001)pc $DyScO_3$ (DSO), and the obtained LNO films were named according to the substrates as displayed in Figure 9a. Correspondingly, a range of strain states from −1.2% to 2.7% was formed on these LNO-loaded substrates. As the strain

changed from 2.7 % to −1.2 %, the OER and ORR activities in alkaline electrolytes increased significantly (Figures 9b and c). The sample with the compressive strain state of −1.2 % displayed the best bifunctional performance with the highest current densities at the overpotential (η) of 400 mV and the lowest total η of 30 μA cm^{-2}, which indicate the potential for use in ZABs. The X-ray linear dichroism data and theoretical calculation results (Figures 9d and e) revealed that the compressive strain induced e_g-orbital splitting and polarization with lower energies and higher e_g-orbital occupancy, which led to weaker M–O chemisorption, and thus, favored the great improvement in the catalytic activity of the perovskites. More recently, Liu's group reported that the compressively strained $La_{0.7}Sr_{0.3}CoO_{3-\delta}$ (LSC) exhibited considerably higher OER activity than the LSC with tensile strain, and it was ascribed to a coupled effect of lattice stain and oxygen defects. They found that the LSC with tensile strain had lower oxygen vacancy formation energy and thus large oxygen deficiency as compared to that with compressive strain. The excessive oxygen vacancy in the tensely strained LSC increased the e_g occupancy and enlarged the energy gap between Co 3d and O 2p band, thus lowering the OER activity[93]. Despite the great potential of the strain tuning strategy, the specific research of strained perovskite in the oxygen electrocatalysis is still relatively limited. Moreover, for different perovskites reported by different groups, the role of tensile and compressive strain on the OER/ORR activity is discrepancy. Therefore, further comprehensive and systematic studies should be considered to reveal the insightful mechanism of the strain-dependent oxygen electrocatalytic activity of perovskite oxides.

3.7 Optimizing the electrode structure

In addition to the previous strategies which improve the intrinsic activity and number of active sites of the electrocatalysts, other strategies that optimize the structure of the air cathode is also critical for the battery performance of ZAB.

Since the ORR reaction occurs at the solid-liquid-air triple-phase boundaries, balancing the hydrophilic and hydrophobic nature of the air cathode is rather significant. To this regard, Zhang's group invented an asymmetric air cathode using a Janus carbon fiber paper. The authors selectively grew the electrocatalysts on the hydrophilic face and retained the blank hydrophobic face. This asymmetric structure allowed a simultaneous O_2 gas diffusion and electrolyte permeation within the carbon skeleton. As a result, a 3D region with abundant triple-phase interfaces was obtained, and thus ORR activity was dramatically improved.[94] Besides, Chen *et al.* combined the hydrophilic $La_{0.5}Sr_{0.5}Co_{0.8}Fe_{0.2}O_3$ perovskite with the hydrophobic N-doped reduced graphene oxide, achieving excellent OER and ORR activity.[95]

Moreover, building self-standing structures for the air cathode of ZAB, especially flexible ZAB, is gaining increasing interest recently. For the conventional fabrication of air cathodes, the electrocatalysts are loading on a substrate such as carbon paper, carbon cloth, or nickel foam. Therefore, the mechanical property of the conventional air cathodes strongly depends on the mechanical properties of their substrates, where the lack of shape diversity may impede their application in wearable devices. Lee *et al.* developed an extremely foldable monolithic heteronanomat (MH) paper that simultaneously realized the hydrophilicity/hydrophobicity balance and an excellent deformability. The MH paper consisted of the $NdBa_{0.5}Sr_{0.5}Co_{1.5}Fe_{0.5}O_{5+\delta}$ double

perovskite (NBSCF), N-doped carbon nanotubes (N-CNT), cellulose nanofibers (CNFs), and polytetrafluoroethylene (PTFE).[96] NBSCF and N-CNT undertook the OER and ORR catalysis, respectively. The hydrophilic CNFs and hydrophobic PTFE constructed interlaced channels for the diffusion of the electrolyte and gas, which helped to create favorable triple-phase boundaries for the ORR. The self-standing MH paper was fabricated via the vacuum filtration of the multicomponent suspension (Figure 10a). The network structure of the MH paper comprised highly entangled 1D and nanoparticle components, which can be distinctly identified in the scanning electron micrograph in Figure 10b. The resultant MH paper exhibited superior mechanical flexibility compared with the commercial air cathode and carbon paper (Figure 10c), and it also retained stable electronic resistance under various deformation modes. Moreover, the MH paper can be directly utilized as air cathode without the use of an additional current collector and gas diffusion layer. Figure 10d displays the water contact angles and discharge voltage test data of the MH paper air cathode with and without PTFE, which reveals the importance of the hydrophobic component for securing air channels and the performance of the battery. The charge–discharge profiles of the flexible ZAB featuring the MH paper were nearly identical in unfolded and fully folded states (Figure 10e). Thus, it was suggested that this MH paper should be further improved and its use should be widened to produce scalable and flexible air cathodes.[96]

4. Conclusion and Outlook

The lack of efficient and inexpensive electrocatalysts for the air cathodes is one of the main reasons that impede the commercialization of ZABs. Among various developed OER/ORR electrocatalysts, perovskite oxides are ideal owing to their flexible and tunable physicochemical properties and low cost. Herein we highlighted the historically important studies and recent developments of perovskite oxides as oxygen electrocatalysts for alkaline ZABs. The catalytic activity and stability for the ORR and OER in ZABs of these as-reported perovskite materials could be easily tuned via the rational design and control of their internal structure and composition, which include phase tailoring, creating various lattice defects, A- or B-site heteroatom doping, favorable morphology design, building hybrid composites, tuning lattice strain, and balancing the hydrophobicity/hydrophilicity. Consequently, these elaborately constructed perovskite structures have demonstrated excellent efficacy in ZABs, and some even outperformed noble metal systems, as described in Table 1. Despite the indisputable success achieved in the development of perovskites for oxygen-related catalysis in ZABs, some challenges still remain, and several difficulties should be overcome in the future to fully unlock the potential of perovskite materials as electrocatalysts.

First, perovskite oxides possess relatively low electronic conductivity, which significantly impairs their electrocatalytic performance on the air electrodes of ZABs. Hence, more attempts should be made at improving their intrinsic conductivity or building hybrids between perovskite oxides and other highly conductive components.

Second, the long-term stability is a critical concern. The highly concentrated alkaline electrolytes and large charge/discharge current densities of ZABs might trigger the degradation of perovskite oxides owing to the gradual transformation of their crystal structure and surface properties. In particular, the segregation of dopants or surface amorphization could be observed at the surface or interfaces of some perovskite-type catalysts. The reconstruction and decomposition of most of these surfaces jeopardize both the activity and stability of the catalysts. Accordingly, it is of paramount importance to stabilize the perovskite structure by introducing stable dopants, such as Ca, Nb, and Sc, or by engineering favorable special morphologies, such as that of the more excellent stability in 3DOM structured $LaFeO_3$ than the bulk counterpart resulting from the optimized Fe/O species.[97]

Third, albeit these proposed design strategies play a critical role in improving the electrochemical performance of perovskite oxides, ideal electrocatalysts are still unattainable. Therefore, fundamental investigations using advanced techniques, such as DFT calculations, *in situ* Raman spectroscopy, and X-ray absorption spectroscopy, are highly required to precisely identify the electrocatalytically active sites of perovskite oxides. Moreover, the fact that electrocatalysis reactions occur at the electrocatalyst-electrolyte-gas interface should be a critical concern when constructing the structure-activity relationship of electrocatalysts. Hence, the development of more surface-sensitive techniques to probe the surface properties of electrocatalysts is highly demanded. In addition to the conventional regulation strategies discussed here, it is expected that researchers would reveal several other effective methods, such as the use

of magnetic fields (plasma sputtering) or external electric fields, to fine modulate the electronic structure of catalysts.

Lastly, more efforts should be paid on the development of perovskite oxides with self-supporting 3D structures and nanoarrays. Electrocatalysts with such structure could offer abundant interconnected channels that are instrumental for the transport of electrons and ions, as well as the accommodation of the reactants and reaction intermediates. Moreover, the 3D structure suppresses the electrode detachment that results from the expansion and contraction of the electrode during the discharge and charge processes. Additionally, self-supporting frameworks eliminate the use of low conductive binders, and thus it would benefit the electron transport and diminish the block of active sites. Therefore, feasible methods for the construction of self-supporting 3D structures and nanoarrays are highly demanded to fully exploit the potential of perovskite oxide-based air cathodes.

Declaration of Competing Interest

The authors declare no competing interests.

Acknowledgements

M. Ni would like to thank the Research Grant Council, University Grants Committee, Hong Kong SAR for the funding (Project Numbers: PolyU 152214/17E and PolyU 152064/18E).

References

[1] H.F. Wang, C. Tang, Q. Zhang, A Review of Precious-Metal-Free Bifunctional Oxygen Electrocatalysts: Rational Design and Applications in Zn− Air Batteries,

Adv. Funct. Mater. 28 (2018) 1803329.
[2] H.-F. Wang, Q. Xu, Materials Design for Rechargeable Metal-Air Batteries, Matter 1 (2019) 565-595.
[3] H. Li, L. Ma, C. Han, Z. Wang, Z. Liu, Z. Tang, C. Zhi, Advanced rechargeable zinc-based batteries: Recent progress and future perspectives, Nano Energy (2019).
[4] M. Wu, G. Zhang, M. Wu, J. Prakash, S. Sun, Rational design of multifuctional air electrodes for rechargeable Zn–Air batteries: Recent progress and future perspectives, Energy Stor. Mater. (2019).
[5] P. Tan, B. Chen, H. Xu, H. Zhang, W. Cai, M. Ni, M. Liu, Z. Shao, Flexible Zn– and Li–air batteries: recent advances, challenges, and future perspectives, Energy Environ. Sci. 10 (2017) 2056-2080.
[6] Z. Zeng, V. Murugesan, K.S. Han, X. Jiang, Y. Cao, L. Xiao, X. Ai, H. Yang, J.-G. Zhang, M.L. Sushko, Non-flammable electrolytes with high salt-to-solvent ratios for Li-ion and Li-metal batteries, Nat. Energy 3 (2018) 674-681.
[7] P. Gu, M. Zheng, Q. Zhao, X. Xiao, H. Xue, H. Pang, Rechargeable zinc–air batteries: a promising way to green energy, J. Mater. Chem. A 5 (2017) 7651-7666.
[8] X. Chen, Z. Zhou, H.E. Karahan, Q. Shao, L. Wei, Y. Chen, Recent advances in materials and design of electrochemically rechargeable zinc–air batteries, Small 14 (2018) 1801929.
[9] J. Yu, Q. He, G. Yang, W. Zhou, Z. Shao, M. Ni, Recent advances and prospective in ruthenium-based materials for electrochemical water splitting, ACS Catal. 9 (2019) 9973-10011.
[10] Y. Zhu, W. Zhou, Z. Shao, Perovskite/carbon composites: applications in oxygen electrocatalysis, Small 13 (2017) 1603793.
[11] J. Yu, R. Ran, Y. Zhong, W. Zhou, M. Ni, Z. Shao, Advances in Porous Perovskites: Synthesis and Electrocatalytic Performance in Fuel Cells and Metal–Air Batteries, Energy Environ. Mater.
[12] X. Xu, W. Wang, W. Zhou, Z. Shao, Recent advances in novel nanostructuring methods of perovskite electrocatalysts for energy-related applications, Small Methods 2 (2018) 1800071.
[13] Y. Sun, X. Liu, Y. Jiang, J. Li, J. Ding, W. Hu, C. Zhong, Recent advances and challenges in divalent and multivalent metal electrodes for metal–air batteries, J. Mater. Chem. A 7 (2019) 18183-18208.
[14] B. Lv, S. Zeng, W. Yang, J. Qiao, C. Zhang, C. Zhu, M. Chen, J. Di, Q. Li, In-situ embedding zeolitic imidazolate framework derived Co–N–C bifunctional catalysts in carbon nanotube networks for flexible Zn–air batteries, J. Energy Chem. 38 (2019) 170-176.
[15] C. Zhu, Y. Ma, W. Zang, C. Guan, X. Liu, S.J. Pennycook, J. Wang, W. Huang, Conformal dispersed cobalt nanoparticles in hollow carbon nanotube arrays for flexible Zn-air and Al-air batteries, Chem. Eng. J. 369 (2019) 988-995.
[16] J. Park, M. Park, G. Nam, J.s. Lee, J. Cho, All-solid-state cable-type flexible zinc–air battery, Adv. Mater. 27 (2015) 1396-1401.

[17] D. Yang, L. Zhang, X. Yan, X. Yao, Recent progress in oxygen electrocatalysts for zinc–air batteries, Small Methods 1 (2017) 1700209.
[18] J. Suntivich, H.A. Gasteiger, N. Yabuuchi, H. Nakanishi, J.B. Goodenough, Y. Shao-Horn, Design principles for oxygen-reduction activity on perovskite oxide catalysts for fuel cells and metal–air batteries, Nat. Chem. 3 (2011) 546-550.
[19] Q. Zhao, Z. Yan, C. Chen, J. Chen, Spinels: controlled preparation, oxygen reduction/evolution reaction application, and beyond, Chem. Rev. 117 (2017) 10121-10211.
[20] J.T. Mefford, X. Rong, A.M. Abakumov, W.G. Hardin, S. Dai, A.M. Kolpak, K.P. Johnston, K.J. Stevenson, Water electrolysis on $La_{1-x}Sr_xCoO_{3-\delta}$ perovskite electrocatalysts, Nat. Commun. 7 (2016) 1-11.
[21] S. She, J. Yu, W. Tang, Y. Zhu, Y. Chen, J. Sunarso, W. Zhou, Z. Shao, Systematic Study of Oxygen Evolution Activity and Stability on $La_{1-x}Sr_xFeO_{3-\delta}$ Perovskite Electrocatalysts in Alkaline Media, ACS Appl. Mater. Interfaces 10 (2018) 11715-11721.
[22] X. Rong, J. Parolin, A.M. Kolpak, A fundamental relationship between reaction mechanism and stability in metal oxide catalysts for oxygen evolution, ACS Catal. 6 (2016) 1153-1158.
[23] S. Gupta, W. Kellogg, H. Xu, X. Liu, J. Cho, G. Wu, Bifunctional perovskite oxide catalysts for oxygen reduction and evolution in alkaline media, Chem. Asian. J. 11 (2016) 10-21.
[24] F. Morin, T. Wolfram, Surface states and catalysis on d-band perovskites, Phys. Rev. Lett. 30 (1973) 1214.
[25] J.B. Goodenough, J.-S. Zhou, Localized to itinerant electronic transitions in transition-metal oxides with the perovskite structure, Chem. Mater. 10 (1998) 2980-2993.
[26] J. Suntivich, K.J. May, H.A. Gasteiger, J.B. Goodenough, Y. Shao-Horn, A perovskite oxide optimized for oxygen evolution catalysis from molecular orbital principles, Science 334 (2011) 1383-1385.
[27] C. Jin, X. Cao, F. Lu, Z. Yang, R. Yang, Electrochemical study of $Ba_{0.5}Sr_{0.5}Co_{0.8}Fe_{0.2}O_3$ perovskite as bifunctional catalyst in alkaline media, Int. J. Hydrogen Energy 38 (2013) 10389-10393.
[28] A. Ashok, A. Kumar, R.R. Bhosale, F. Almomani, S.S. Malik, S. Suslov, F. Tarlochan, Combustion synthesis of bifunctional $LaMO_3$ (M= Cr, Mn, Fe, Co, Ni) perovskites for oxygen reduction and oxygen evolution reaction in alkaline media, J. Electroanal. Chem. 809 (2018) 22-30.
[29] Y.-Q. Lyu, F. Ciucci, Activating the bifunctionality of a perovskite oxide toward oxygen reduction and oxygen evolution reactions, ACS Appl. Mater. Interfaces 9 (2017) 35829-35836.
[30] J. Hu, L. Wang, L. Shi, H. Huang, Oxygen reduction reaction activity of $LaMn_{1-x}Co_xO_3$-graphene nanocomposite for zinc-air battery, Electrochim. Acta 161 (2015) 115-123.
[31] F. Lu, J. Sui, J. Su, C. Jin, M. Shen, R. Yang, Hollow spherical $La_{0.8}Sr_{0.2}MnO_3$ perovskite oxide with enhanced catalytic activities for the oxygen reduction

reaction, J. Power Sources 271 (2014) 55-59.
[32] J. Yu, J. Sunarso, Y. Zhu, X. Xu, R. Ran, W. Zhou, Z. Shao, Activity and stability of Ruddlesden–Popper-type $La_{n+1}Ni_nO_{3n+1}$ (n= 1, 2, 3, and∞) electrocatalysts for oxygen reduction and evolution reactions in alkaline media, Chem. Eur. J. 22 (2016) 2719-2727.
[33] A. Vignesh, M. Prabu, S. Shanmugam, Porous $LaCo_{1-x}Ni_xO_{3-\delta}$ Nanostructures as an Efficient Electrocatalyst for Water Oxidation and for a Zinc–Air Battery, ACS Appl. Mater. Interfaces 8 (2016) 6019-6031.
[34] I. Yamada, H. Fujii, A. Takamatsu, H. Ikeno, K. Wada, H. Tsukasaki, S. Kawaguchi, S. Mori, S. Yagi, Bifunctional oxygen reaction catalysis of quadruple manganese perovskites, Adv. Mater. 29 (2017) 1603004.
[35] B. Hua, Y.-F. Sun, M. Li, N. Yan, J. Chen, Y.-Q. Zhang, Y. Zeng, B. Shalchi Amirkhiz, J.-L. Luo, Stabilizing double perovskite for effective bifunctional oxygen electrocatalysis in alkaline conditions, Chem. Mater. 29 (2017) 6228-6237.
[36] H. Lee, O. Gwon, C. Lim, J. Kim, O. Galindev, G. Kim, Advanced electrochemical properties of $PrBa_{0.5}Sr_{0.5}Co_{1.9}Ni_{0.1}O_{5+\delta}$ as a bifunctional catalyst for rechargeable zinc-air batteries, ChemElectroChem 6 (2019) 3154-3159.
[37] M. Retuerto, F. Calle-Vallejo, L. Pascual, G. Lumbeeck, M.T. Fernandez-Diaz, M. Croft, J. Gopalakrishnan, M.A. Pena, J. Hadermann, M. Greenblatt, $La_{1.5}Sr_{0.5}NiMn_{0.5}Ru_{0.5}O_6$ double perovskite with enhanced ORR/OER bifunctional catalytic activity, ACS Appl. Mater. Interfaces 11 (2019) 21454-21464.
[38] M.A. Kirsanova, V.D. Okatenko, D.A. Aksyonov, R.P. Forslund, J.T. Mefford, K.J. Stevenson, A.M. Abakumov, Bifunctional OER/ORR catalytic activity in the tetrahedral $YBaCo_4O_{7.3}$ oxide, J. Mater. Chem. A 7 (2019) 330-341.
[39] G. Ou, C. Yang, Y. Liang, N. Hussain, B. Ge, K. Huang, Y. Xu, H. Wei, R. Zhang, H. Wu, Surface engineering of perovskite oxide for bifunctional oxygen electrocatalysis, Small Methods 3 (2019) 1800279.
[40] J. Bian, Z. Li, N. Li, C. Sun, Oxygen deficient $LaMn_{0.75}Co_{0.25}O_{3-\delta}$ nanofibers as an efficient electrocatalyst for oxygen evolution reaction and zinc–air batteries, Inorg. Chem. 58 (2019) 8208-8214.
[41] J.I. Jung, S. Park, M.G. Kim, J. Cho, Tunable internal and surface structures of the bifunctional oxygen perovskite catalysts, Adv. Energy Mater. 5 (2015) 1501560.
[42] W. Zhou, R. Ran, Z. Shao, W. Zhuang, J. Jia, H. Gu, W. Jin, N. Xu, Barium-and strontium-enriched $(Ba_{0.5}Sr_{0.5})_{1+x}Co_{0.8}Fe_{0.2}O_{3-\delta}$ oxides as high-performance cathodes for intermediate-temperature solid-oxide fuel cells, Acta Mater. 56 (2008) 2687-2698.
[43] W. Xu, N. Apodaca, H. Wang, L. Yan, G. Chen, M. Zhou, D. Ding, P. Choudhury, H. Luo, A-site Excessive $(La_{0.8}Sr_{0.2})_{1+x}MnO_3$ Perovskite Oxides for Bifunctional Oxygen Catalyst in Alkaline Media, ACS Catal. 9 (2019) 5074-5083.
[44] Y. Zhu, W. Zhou, J. Yu, Y. Chen, M. Liu, Z. Shao, Enhancing electrocatalytic activity of perovskite oxides by tuning cation deficiency for oxygen reduction and evolution reactions, Chemistry of Materials 28 (2016) 1691-1697.

[45] B. Niu, F. Jin, T. Feng, L. Zhang, Y. Zhang, T. He, A-site deficient $(La_{0.6}Sr_{0.4})_{1-x}Co_{0.2}Fe_{0.6}Nb_{0.2}O_{3-\delta}$ symmetrical electrode materials for solid oxide fuel cells, Electrochim. Acta 270 (2018) 174-182.
[46] R.-h. Yuan, Y. He, W. He, M. Ni, M.K. Leung, Bifunctional electrocatalytic activity of $La_{0.8}Sr_{0.2}MnO_3$-based perovskite with the A-site deficiency for oxygen reduction and evolution reactions in alkaline media, Appl. Energy 251 (2019) 113406.
[47] J.I. Jung, H.Y. Jeong, M.G. Kim, G. Nam, J. Park, J. Cho, Fabrication of $Ba_{0.5}Sr_{0.5}Co_{0.8}Fe_{0.2}O_{3-\delta}$ catalysts with enhanced electrochemical performance by removing an inherent heterogeneous surface film layer, Adv. Mater. 27 (2015) 266-271.
[48] N.-L. Wu, W.-R. Liu, S.-J. Su, Effect of oxygenation on electrocatalysis of $La_{0.6}Ca_{0.4}CoO_{3-x}$ in bifunctional air electrode, Electrochim. Acta 48 (2003) 1567-1571.
[49] B.-Q. Li, Z.-J. Xia, B. Zhang, C. Tang, H.-F. Wang, Q. Zhang, Regulating p-block metals in perovskite nanodots for efficient electrocatalytic water oxidation, Nat. Commun. 8 (2017) 1-7.
[50] Q. Wang, Y. Xue, S. Sun, S. Li, H. Miao, Z. Liu, $La_{0.8}Sr_{0.2}Co_{1-x}Mn_xO_3$ perovskites as efficient bi-functional cathode catalysts for rechargeable zinc-air batteries, Electrochim. Acta 254 (2017) 14-24.
[51] S. Bie, Y. Zhu, J. Su, C. Jin, S. Liu, R. Yang, J. Wu, One-pot fabrication of yolk–shell structured $La_{0.9}Sr_{0.1}CoO_3$ perovskite microspheres with enhanced catalytic activities for oxygen reduction and evolution reactions, J. Mater. Chem. A 3 (2015) 22448-22453.
[52] F. Azizi, A. Kahoul, A. Azizi, Effect of La doping on the electrochemical activity of double perovskite oxide Sr_2FeMoO_6 in alkaline medium, J. Alloys Compd. 484 (2009) 555-560.
[53] J.-I. Jung, M. Risch, S. Park, M.G. Kim, G. Nam, H.-Y. Jeong, Y. Shao-Horn, J. Cho, Optimizing nanoparticle perovskite for bifunctional oxygen electrocatalysis, Energy Environ. Sci. 9 (2016) 176-183.
[54] D.U. Lee, M.G. Park, H.W. Park, M.H. Seo, V. Ismayilov, R. Ahmed, Z. Chen, Highly active Co-doped $LaMnO_3$ perovskite oxide and N-doped carbon nanotube hybrid bi-functional catalyst for rechargeable zinc–air batteries, Electrochem. Commun. 60 (2015) 38-41.
[55] K. Bradley, K. Giagloglou, B.E. Hayden, H. Jungius, C. Vian, Reversible perovskite electrocatalysts for oxygen reduction/oxygen evolution, Chem. Sci. 10 (2019) 4609-4617.
[56] Y. Bu, O. Gwon, G. Nam, H. Jang, S. Kim, Q. Zhong, J. Cho, G. Kim, A highly efficient and robust cation ordered perovskite oxide as a bifunctional catalyst for rechargeable zinc-air batteries, ACS Nano 11 (2017) 11594-11601.
[57] B. Hua, Y.Q. Zhang, N. Yan, M. Li, Y.F. Sun, J. Chen, J. Li, J.L. Luo, The excellence of both worlds: developing effective double perovskite oxide catalyst of oxygen reduction reaction for room and elevated temperature applications, Adv.

Funct. Mater. 26 (2016) 4106-4112.
[58] Y. Zhu, W. Zhou, Y. Chen, J. Yu, X. Xu, C. Su, M.O. Tadé, Z. Shao, Boosting oxygen reduction reaction activity of palladium by stabilizing its unusual oxidation states in perovskite, Chem. Mater. 27 (2015) 3048-3054.
[59] Y. Shen, Y. Zhu, J. Sunarso, D. Guan, B. Liu, H. Liu, W. Zhou, Z. Shao, New Phosphorus-Doped Perovskite Oxide as an Oxygen Reduction Reaction Electrocatalyst in an Alkaline Solution, Chem. Eur. J. 24 (2018) 6950-6957.
[60] S. Royer, D. Duprez, F. Can, X. Courtois, C. Batiot-Dupeyrat, S. Laassiri, H. Alamdari, Perovskites as substitutes of noble metals for heterogeneous catalysis: dream or reality, Chem. Rev. 114 (2014) 10292-10368.
[61] Y.-C. Lee, P.-Y. Peng, W.-S. Chang, C.-M. Huang, Hierarchical meso-macroporous $LaMnO_3$ electrode material for rechargeable zinc–air batteries, J. Taiwan Inst. Chem. Eng. 45 (2014) 2334-2339.
[62] F. Lu, Y. Wang, C. Jin, F. Li, R. Yang, F. Chen, Microporous $La_{0.8}Sr_{0.2}MnO_3$ perovskite nanorods as efficient electrocatalysts for lithium–air battery, J. Power Sources 293 (2015) 726-733.
[63] Y.-F. Sun, Y.-Q. Zhang, Y.-L. Yang, J. Chen, B. Hua, Y.-X. Shi, C.-A. Wang, J.-L. Luo, Smart tuning of 3D ordered electrocatalysts for enhanced oxygen reduction reaction, Appl. Catal. B 219 (2017) 640-644.
[64] H. Yu, F. Chu, X. Zhou, J. Ji, Y. Liu, Y. Bu, Y. Kong, Y. Tao, Y. Li, Y. Qin, A perovskite oxide with a tunable pore-size derived from a general salt-template strategy as a highly efficient electrocatalyst for the oxygen evolution reaction, Chem. Commun. 55 (2019) 2445-2448.
[65] T. Ishihara, L. Guo, T. Miyano, Y. Inoishi, K. Kaneko, S. Ida, Mesoporous $La_{0.6}Ca_{0.4}CoO_3$ perovskites with large surface areas as stable air electrodes for rechargeable Zn–air batteries, J. Mater. Chem. A 6 (2018) 7686-7692.
[66] H. Wang, J. Wang, Y. Pi, Q. Shao, Y. Tan, X. Huang, Double Perovskite $LaFexNi_{1-x}O_3$ nanorods enable efficient oxygen evolution electrocatalysis, Angew. Chem. 131 (2019) 2338-2342.
[67] X. Ge, F.T. Goh, B. Li, T.A. Hor, J. Zhang, P. Xiao, X. Wang, Y. Zong, Z. Liu, Efficient and durable oxygen reduction and evolution of a hydrothermally synthesized $La(Co_{0.55}Mn_{0.45})_{0.99}\ O_{3-\delta}$ nanorod/graphene hybrid in alkaline media, Nanoscale 7 (2015) 9046-9054.
[68] A. Greiner, J.H. Wendorff, Electrospinning: a fascinating method for the preparation of ultrathin fibers, Angew. Chem. Int. Ed. 46 (2007) 5670-5703.
[69] Y. Bu, G. Nam, S. Kim, K. Choi, Q. Zhong, J. Lee, Y. Qin, J. Cho, G. Kim, A Tailored Bifunctional Electrocatalyst: Boosting Oxygen Reduction/Evolution Catalysis via Electron Transfer Between N-Doped Graphene and Perovskite Oxides, Small 14 (2018) 1802767.
[70] Y. Bu, H. Jang, O. Gwon, S.H. Kim, S.H. Joo, G. Nam, S. Kim, Y. Qin, Q. Zhong, S.K. Kwak, Synergistic interaction of perovskite oxides and N-doped graphene in versatile electrocatalyst, J. Mater. Chem. A 7 (2019) 2048-2054.
[71] J. Bian, R. Su, Y. Yao, J. Wang, J. Zhou, F. Li, Z.L. Wang, C. Sun, Mg doped perovskite $LaNiO_3$ nanofibers as an efficient bifunctional catalyst for

rechargeable zinc–air batteries, ACS Appl. Energy Mater. 2 (2019) 923-931.
[72] S. Peng, X. Han, L. Li, S. Chou, D. Ji, H. Huang, Y. Du, J. Liu, S. Ramakrishna, Electronic and defective engineering of electrospun $CaMnO_3$ nanotubes for enhanced oxygen electrocatalysis in rechargeable zinc–air batteries, Adv. Energy Mater. 8 (2018) 1800612.
[73] B. Cai, K. Akkiraju, W.P. Mounfield III, Z. Wang, X. Li, B. Huang, S. Yuan, D. Su, Y. Román-Leshkov, Y. Shao-Horn, Solid-state gelation for nanostructured perovskite oxide aerogels, Chem. Mater. 31 (2019) 9422-9429.
[74] L. Kuai, E. Kan, W. Cao, M. Huttula, S. Ollikkala, T. Ahopelto, A.-P. Honkanen, S. Huotari, W. Wang, B. Geng, Mesoporous $LaMnO_{3+\delta}$ perovskite from spray−pyrolysis with superior performance for oxygen reduction reaction and Zn−air battery, Nano Energy 43 (2018) 81-90.
[75] X. Zhu, Z. Liu, N. Ming, Perovskite oxide nanotubes: synthesis, structural characterization, properties and applications, J. Mater. Chem. 20 (2010) 4015-4030.
[76] J. Liu, D. Zhu, Y. Zheng, A. Vasileff, S.-Z. Qiao, Self-supported earth-abundant nanoarrays as efficient and robust electrocatalysts for energy-related reactions, ACS Catal. 8 (2018) 6707-6732.
[77] Y. Gao, J. Wang, Y.-Q. Lyu, K. Lam, F. Ciucci, In situ growth of Pt_3Ni nanoparticles on an A-site deficient perovskite with enhanced activity for the oxygen reduction reaction, J. Mater. Chem. A 5 (2017) 6399-6404.
[78] X. Wang, J. Sunarso, Q. Lu, Z. Zhou, J. Dai, D. Guan, W. Zhou, Z. Shao, High-Performance Platinum-Perovskite Composite Bifunctional Oxygen Electrocatalyst for Rechargeable Zn–Air Battery, Adv. Energy Mater. 10 (2020) 1903271.
[79] Z. Yan, H. Sun, X. Chen, X. Fu, C. Chen, F. Cheng, J. Chen, Rapid low-temperature synthesis of perovskite/carbon nanocomposites as superior electrocatalysts for oxygen reduction in Zn-air batteries, Nano Research 11 (2018) 3282-3293.
[80] C.-F. Chen, G. King, R.M. Dickerson, P.A. Papin, S. Gupta, W.R. Kellogg, G. Wu, Oxygen-deficient $BaTiO_{3-x}$ perovskite as an efficient bifunctional oxygen electrocatalyst, Nano Energy 13 (2015) 423-432.
[81] J. Hu, Q. Liu, Z. Shi, L. Zhang, H. Huang, $LaNiO_3$-nanorod/graphene composite as an efficient bi-functional catalyst for zinc–air batteries, RSC Adv. 6 (2016) 86386-86394.
[82] D.-G. Lee, S.H. Kim, S.H. Joo, H.-I. Ji, H. Tavassol, Y. Jeon, S. Choi, M.-H. Lee, C. Kim, S.K. Kwak, Polypyrrole-assisted oxygen electrocatalysis on perovskite oxides, Energy Environ. Sci. 10 (2017) 523-527.
[83] Y.-Q. Zhang, H.-B. Tao, Z. Chen, M. Li, Y.-F. Sun, B. Hua, J.-L. Luo, In situ grown cobalt phosphide (CoP) on perovskite nanofibers as an optimized trifunctional electrocatalyst for Zn–air batteries and overall water splitting, J. Mater. Chem. A 7 (2019) 26607-26617.
[84] L. Gui, Z. Wang, K. Zhang, B. He, Y. Liu, W. Zhou, J. Xu, Q. Wang, L. Zhao, Oxygen vacancies-rich $Ce_{0.9}Gd_{0.1}O_{2-\delta}$ decorated $Pr_{0.5}Ba_{0.5}CoO_{3-\delta}$ bifunctional

catalyst for efficient and long-lasting rechargeable Zn-air batteries, Appl. Catal. B 266 (2020) 118656.
[85] R. Majee, Q.A. Islam, S. Bhattacharyya, Surface Charge Modulation of Perovskite Oxides at the Crystalline Junction with Layered Double Hydroxide for a Durable Rechargeable Zinc–Air Battery, ACS Appl. Mater. Interfaces 11 (2019) 35853-35862.
[86] S. She, Y. Zhu, Y. Chen, Q. Lu, W. Zhou, Z. Shao, Realizing ultrafast oxygen evolution by introducing proton acceptor into perovskites, Adv. Energy Mater. 9 (2019) 1900429.
[87] S. Yan, Y. Xue, S. Li, G. Shao, Z. Liu, Enhanced Bifunctional Catalytic Activity of Manganese Oxide/Perovskite Hierarchical Core–Shell Materials by Adjusting the Interface for Metal–Air Batteries, ACS Appl. Mater. Interfaces 11 (2019) 25870-25881.
[88] X. Wang, Z. Pan, X. Chu, K. Huang, Y. Cong, R. Cao, R. Sarangi, L. Li, G. Li, S. Feng, Atomic-Scale Insights into Surface Lattice Oxygen Activation at the Spinel/Perovskite interface of $Co_3O_4/La_{0.3}Sr_{0.7}CoO_3$, Angew. Chem. 131 (2019) 11846-11851.
[89] M. Kubicek, Z. Cai, W. Ma, B. Yildiz, H. Hutter, J. Fleig, Tensile Lattice Strain Accelerates Oxygen Surface Exchange and Diffusion in $La_{1-x}Sr_xCoO_{3-\delta}$ Thin Films, ACS Nano 7 (2013) 3276-3286.
[90] P. Strasser, S. Koh, T. Anniyev, J. Greeley, K. More, C. Yu, Z. Liu, S. Kaya, D. Nordlund, H. Ogasawara, Lattice-strain control of the activity in dealloyed core–shell fuel cell catalysts, Nat. Chem. 2 (2010) 454.
[91] K.A. Stoerzinger, W.S. Choi, H. Jeen, H.N. Lee, Y. Shao-Horn, Role of strain and conductivity in oxygen electrocatalysis on $LaCoO_3$ thin films, J. Phys. Chem. Lett. 6 (2015) 487-492.
[92] J.R. Petrie, V.R. Cooper, J.W. Freeland, T.L. Meyer, Z. Zhang, D.A. Lutterman, H.N. Lee, Enhanced bifunctional oxygen catalysis in strained $LaNiO_3$ perovskites, J. Am. Chem. Soc. 138 (2016) 2488-2491.
[93] X. Liu, L. Zhang, Y. Zheng, Z. Guo, Y. Zhu, H. Chen, F. Li, P. Liu, B. Yu, X. Wang, Uncovering the effect of lattice strain and oxygen deficiency on electrocatalytic activity of perovskite cobaltite thin films, Adv. Sci. 6 (2019) 1801898.
[94] J. Yu, B.Q. Li, C.X. Zhao, J.N. Liu, Q. Zhang, Asymmetric Air Cathode Design for Enhanced Interfacial Electrocatalytic Reactions in High-Performance Zinc–Air Batteries, Adv. Mater. (2020).
[95] H.W. Park, D.U. Lee, P. Zamani, M.H. Seo, L.F. Nazar, Z. Chen, Electrospun porous nanorod perovskite oxide/nitrogen-doped graphene composite as a bi-functional catalyst for metal air batteries, Nano Energy 10 (2014) 192-200.
[96] D. Lee, H. Lee, O. Gwon, O. Kwon, H.Y. Jeong, G. Kim, S.-Y. Lee, Monolithic heteronanomat paper air cathodes toward origami-foldable/rechargeable Zn–air batteries, J. Mater. Chem. A 7 (2019) 24231-24238.
[97] J. Dai, Y. Zhu, Y. Zhong, J. Miao, B. Lin, W. Zhou, Z. Shao, Enabling High and Stable Electrocatalytic Activity of Iron-Based Perovskite Oxides for Water

Splitting by Combined Bulk Doping and Morphology Designing, Adv. Mater. Interfaces 6 (2019) 1801317.

Table

Table 1. Performance and durability of Zn–air batteries featuring perovskite oxide-based air cathodes.

Material	Synthesis method	Loading amount	Peak power density (mW cm^{-2})	Voltage gap	Cycle durability	Ref.
$La(Co_{0.71}Ni_{0.25})_{0.96}O_{3-\delta}$	Electrospinning	0.4 mg cm^{-2}	–	Initial 0.529 V (5 A g^{-1})	Voltage gap 0.792 V after 20 cycles (5 A g^{-1})	[33]
$PrBa_{0.5}Sr_{0.5}Co_{2-x}Ni_xO_{5+\delta}$	Sol–gel	1 mg cm^{-2}	–	Initial ~0.75 V (1 mA cm^{-2})	Voltage gap ~0.8 V after 20 cycles (1 mA cm^{-2})	[36]
$(La_{0.8}Sr_{0.2})_{0.95}Mn_{0.5}Fe_{0.5}O_3$	Sol–gel	2 mg cm^{-2}	105	Initial 0.88 V (10 mA cm^{-2})	Voltage gap 1 V after 100 cycles (10 mA cm^{-2})	[46]
$LaMn_{0.75}Co_{0.25}O_{3-\delta}$	Sol–gel	1 mg cm^{-2}	35	Initial ~0.95 V (2 mA cm^{-2})	Voltage gap ~1.05 V after 70 h (2 mA cm^{-2})	[40]
$La_{0.7}(Ba_{0.5}Sr_{0.5})_{0.3}Co_{0.8}Fe_{0.2}O_{3-\delta}$ (50nm)	Sol–gel	0.639 mg cm^{-2}	–	Initial 0.75 V (10.5 mA cm^{-2})	Voltage gap 1.0 V after 100 cycles (10.5 mA cm^{-2})	[53]
$La_{0.8}Sr_{0.2}Co_{0.4}Mn_{0.6}O_3$	Sol–gel	5 mg cm^{-2}	160	Initial ~0.6 V (10 mA cm^{-2})	Voltage gap ~0.78 V after ~16 h (10 mA cm^{-2})	[50]
$LaNi_{0.85}Mg_{0.15}O_3$ nanofiber	Electrospinning	1 mg cm^{-2}	45	Initial 0.92 V (10 mA cm^{-2})	Voltage gap 1.3 V after 110 h (10 mA cm^{-2})	[71]
$Gd_{0.1}Ce_{0.9}O_{2-\delta}$-decorated $(Pr_{0.5}Ba_{0.5})CoO_{3-\delta}$	Infiltration	1 mg cm^{-2}	207	Initial 0.82 V (10 mA cm^{-2})	Voltage gap 0.78 V after 200 h (10 mA cm^{-2})	[84]
S-doped $CaMnO_3$	Electrospinning	0.8 mg cm^{-2}	152	Initial 0.67 (5 mA cm^{-2})	Voltage gap 0.8 V after 13 h (5 mA cm^{-2})	[72]
Pt-$Sr(Co_{0.8}Fe_{0.2})_{0.95}P_{0.05}O_{3-\delta}$ (SCFP)/C	Ball milling	2 mg cm^{-2}	122	Initial 0.77 (5 mA cm^{-2})	Voltage gap 0.86 V after 80 h (5 mA cm^{-2})	[78]
$La_{0.99}MnO_{3.03}$/C nanocomposite	Gel auto-combustion synthesis	1 mg cm^{-2}	430	–	–	[79]
$La_{0.7}Sr_{0.3}MnO_3$-MnO_2	In situ dissolving	–	181.4	Initial 0.793 V (10 mA cm^{-2})	Voltage gap 0.949 V after 8 h (10 mA cm^{-2})	[87]
CoP-$PrBa_{0.5}Sr_{0.5}Co_{1.5}Fe_{0.5}O_{5+\delta}$	In situ exclusion followed by post growth	0.5 mg cm^{-1}	138	Initial 0.84 V (10 mA cm^{-2})	Voltaic efficiency of 58.3% after 33 h (10 mA cm^{-2})	[83]
$(PrBa_{0.5}Sr_{0.5})_{0.95}Co_{1.5}Fe_{0.5}O_{5+\delta}$-3D N-doped graphene	Coaxial electrospinning	–	128.5	Initial 0.88 V (10 mA cm^{-2})	Voltage gap 0.63 V after 18 h (10 mA cm^{-2})	[70]

Figures

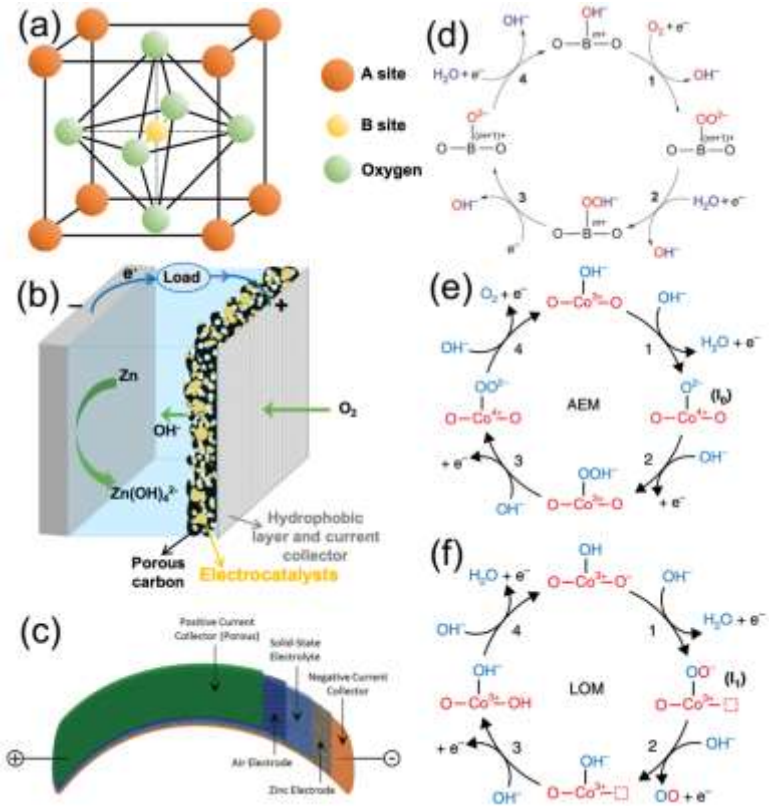

Figure 1 (a) Schematic illustration of ideal unit cell of perovskite oxide. Typical configurations of (b) conventional liquid Zn–air batteries (ZABs) and (c) flexible solid-state ZABs. Reproduced with permission from Ref. [5], © Wiley-VCH 2017. (d) Proposed oxygen reduction reaction pathway on perovskite oxides. Reproduced with permission from Ref. [18], © Springer Nature 2011. Proposed oxygen evolution reaction pathway on perovskite oxides with (e) absorbate evolution and (f) lattice oxygen participated mechanisms. Reproduced with permission from Ref. [20], © Springer Nature 2016.

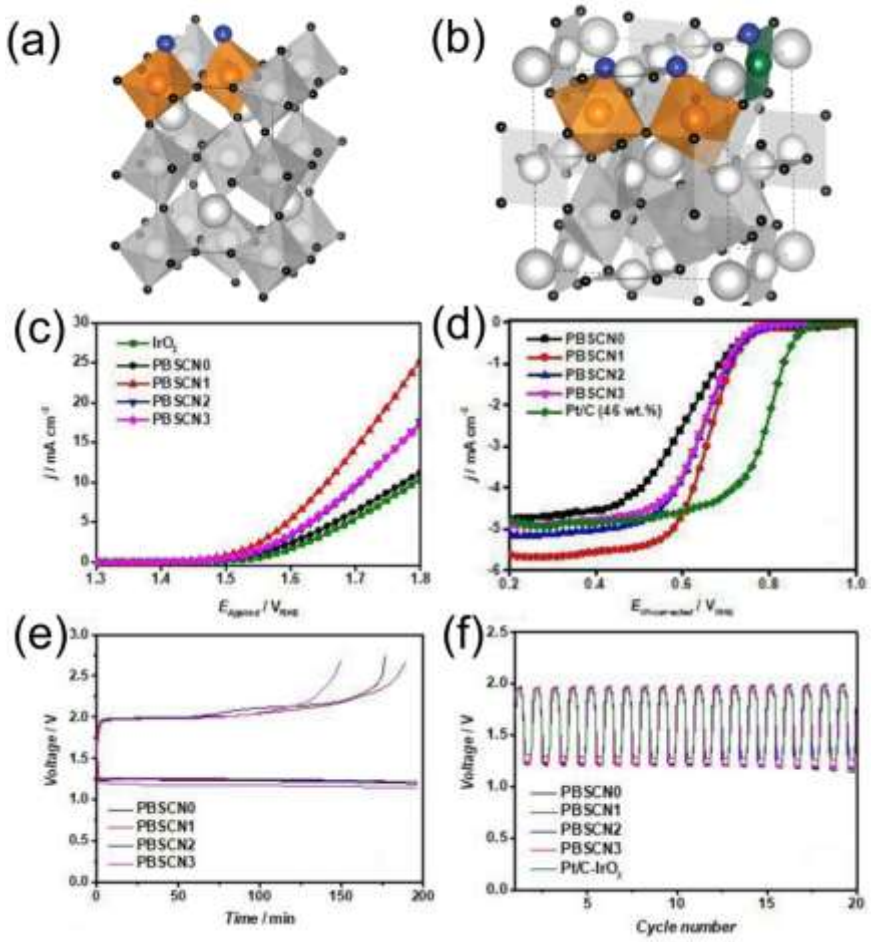

Figure 2 Schematic illustration of crystal structures of (a) single and (b) quadruple perovskite oxides. Reproduced with permission from Ref.[34], © Wiley-VCH 2016. (c) Oxygen evolution reaction (OER) and (d) oxygen reduction reaction (ORR) polarization curves of $PrBa_{0.5}Sr_{0.5}Co_{2-x}Ni_xO_{5+\delta}$ (x = 0, 0.1, 0.2, 0.3) perovskite oxides and IrO_2 and Pt/C benchmark catalysts for the OER and ORR, respectively, in 0.1 M KOH solution. (e) Initial discharge–charge profiles and (f) galvanostatic discharge–charge cycling curves of all reported perovskite oxides at the fixed current density of 1 mA cm^{-2}. During cycling testing, the Pt/C-IrO_2 couple was used as reference. Reproduced with permission from Ref. [36], © Wiley-VCH 2019.

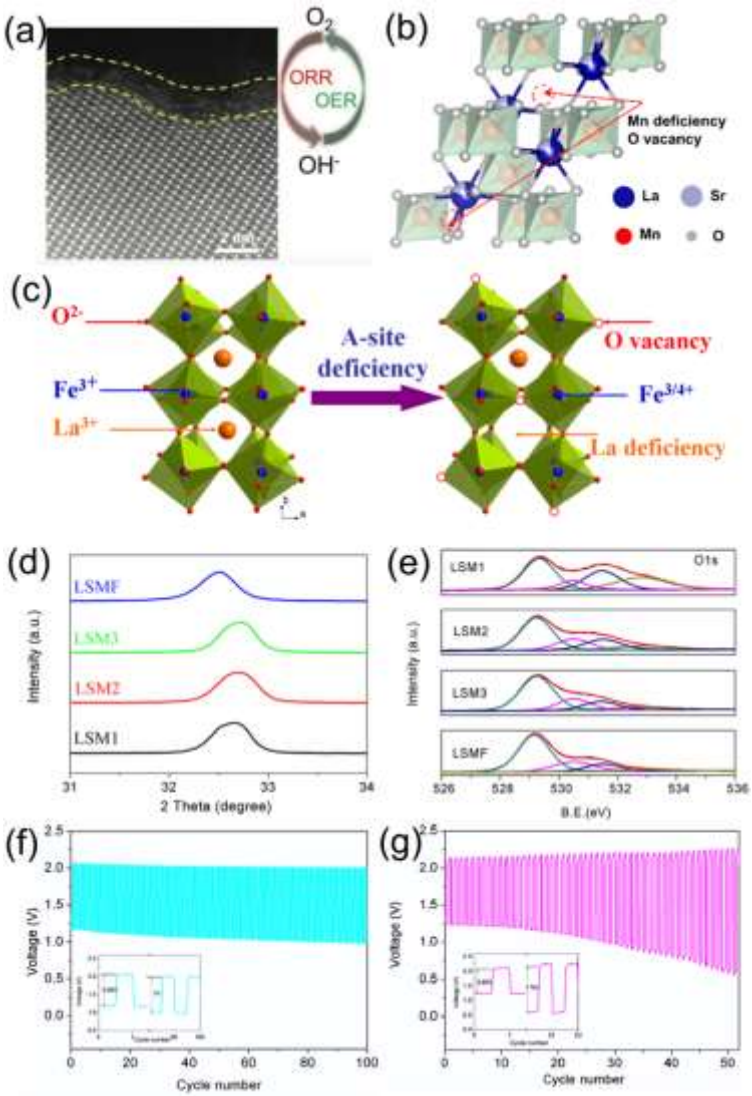

Figure 3 (a) Transmission electron micrograph of the disordered layer that formed on the surface of $La_{0.6}Sr_{0.4}Co_{0.2}Fe_{0.8}O_{3-\delta}$ after $La_{0.6}Sr_{0.4}Co_{0.2}Fe_{0.8}O_{3-\delta}$ underwent Li reduction. Reproduced with permission from Ref. [39], © Wiley-VCH 2018. (b) $(La_{0.8}Sr_{0.2})_{1-x}MnO_3$ perovskite oxide with Mn and O deficiencies. Reproduced with permission from Ref. [43], © American Chemical Society 2019. (c) Schematic illustration of the formation of oxygen vacancy and Fe^{4+} in A-site-deficient $La_{1-x}Fe\ O_{3-\delta}$ perovskites. Reproduced with permission from Ref.[44] © American Chemical Society 2016. (d) Magnified X-ray diffraction patterns of LSM1, LSM2, LSM3, and LSMF. (e) O 1s X-ray photoelectron spectroscopy profiles of LSM1, LSM2, LSM3, and LSMF. Discharge–charge cycling curves of (f) LSMF and (g) Pt/C samples at the fixed current density of 10 mA cm^{-2}. Here LSM1, LSM2, and LSM3, denote $(La_{0.8}Sr_{0.2})_{1-x}MnO_3$ (x = 0, 0.02, 0.05) and LSMF denotes LSM3 where the B-site Mn cations were partially replaced by Fe. Reproduced with permission from Ref. [46], © Elsevier 2019.

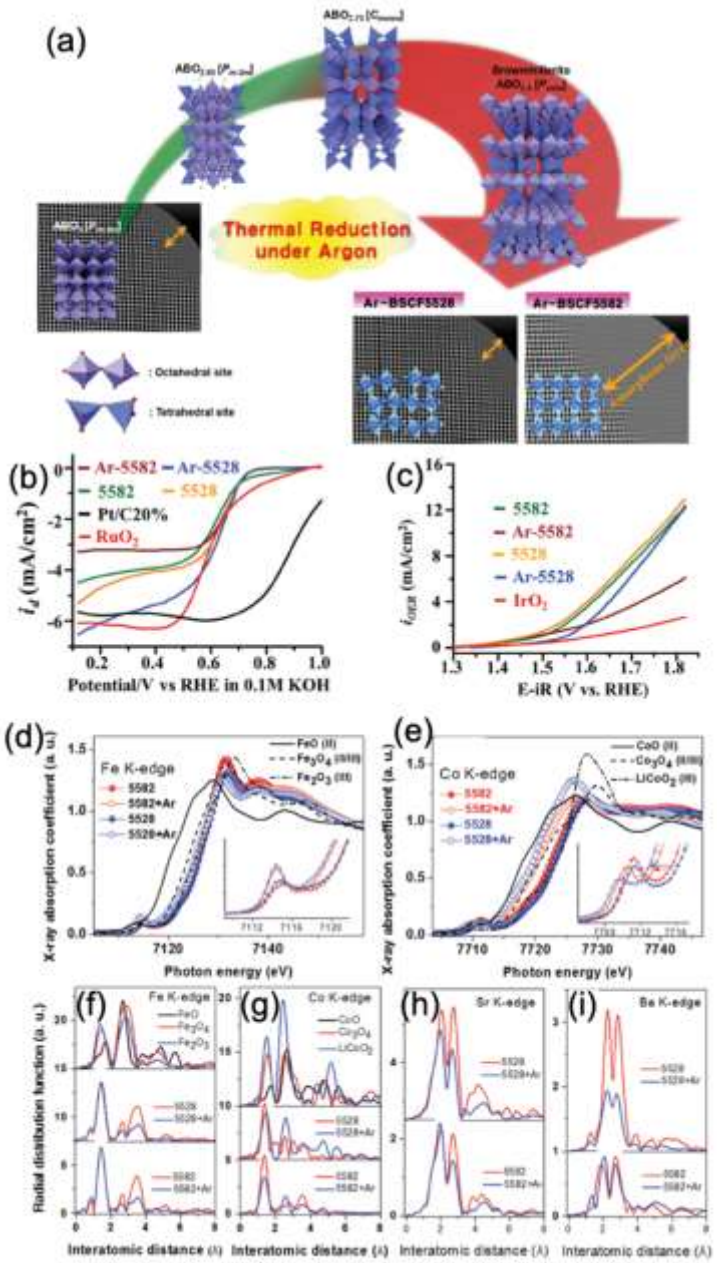

Figure 4 (a) Schematic diagram of surface structure changes of BSCF5582 and BSCF5528 catalysts treated at 950 °C under Ar atmosphere. Linear sweep voltammetry curves toward the (b) oxygen reduction reaction (ORR) and (c) oxygen evolution reaction (OER) of BSCF5582, BSCF5528, BSCF5582-Ar, and BSCF5528-Ar catalysts under alkaline conditions at the rotation rate of 1600 rpm. Pt/C and IrO_2 were selected as ORR and OER benchmark catalysts, respectively. (d) Fe and (e) Co K-edge X-ray absorption near edge structure spectra of BSCF5582, BSCF5528, BSCF5582-Ar, and BSCF5528-Ar. Radial distribution function of (f) Fe, (g) Co, (h) Sr, and (i) Ba K-edge extended X-ray absorption fine structure spectra for varied catalysts. Reproduced with permission from Ref. [41], © Wiley-VCH 2015. Here BSCF5528 and BSCF5528 denote $Ba_{0.5}Sr_{0.5}Co_xFe_{1-x}O_{3-\delta}$ (x = 0.2 and 0.8), and BSCF5528-Ar, and BSCF5582-Ar denote BSCF5528 and BSCF5528 that were heat-treated at 950 °C under the Ar atmosphere, respectively.

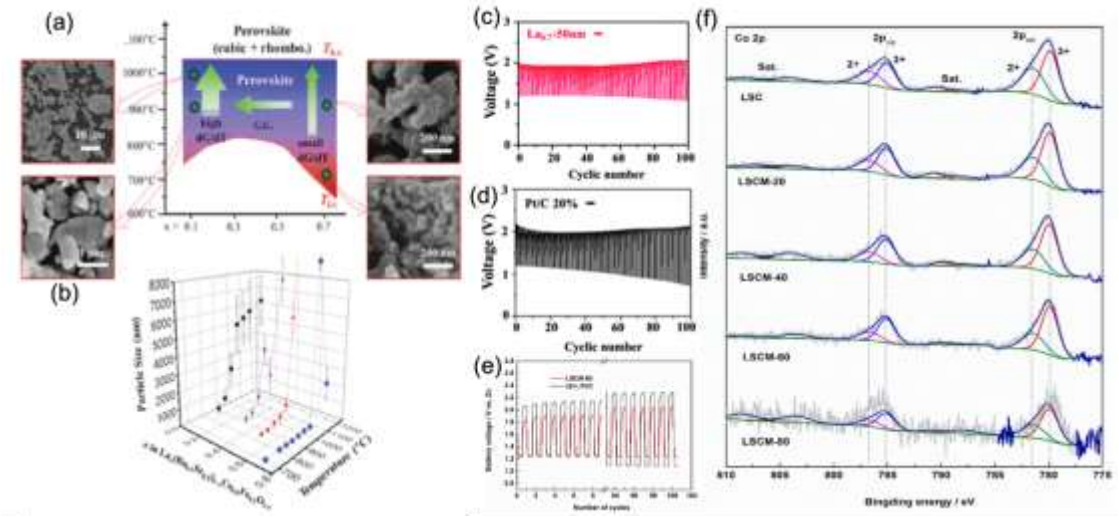

Figure 5 (a) Phase structure vs. La doping amount and calcination temperatures, in which the stable cubic phase was obtained between the high and low critical temperatures ($T_{h.c}$ and $T_{l.c}$, respectively.). Particle size was increased along the arrow direction. (b) Phase diagram of particle size vs. La doping amount and calcination temperatures. Galvanostatic charge–discharge cycling curves of (c) $La_{0.7}$-50 nm and (d) Pt/C samples at 10.5 mA cm^{-2}. Reproduced with permission from Ref.[53], © Royal Society of Chemistry 2016. (e) Charge–discharge stability tests of ZABs using LSCM-60 and Pt/C as cathode catalysts at 10 mA cm^{-2} and 10 min cycles. (f) XPS spectra of Co 2p of LSCM with various Mn doping level. Reproduced with permission from Ref. [50], © Elsevier 2017. Here $La_{0.7}$-50 nm denotes La-doped $Ba_{0.5}Sr_{0.5}Co_xFe_{1-x}O_{3-\delta}$ perovskite with very small particles (~50 nm in size).

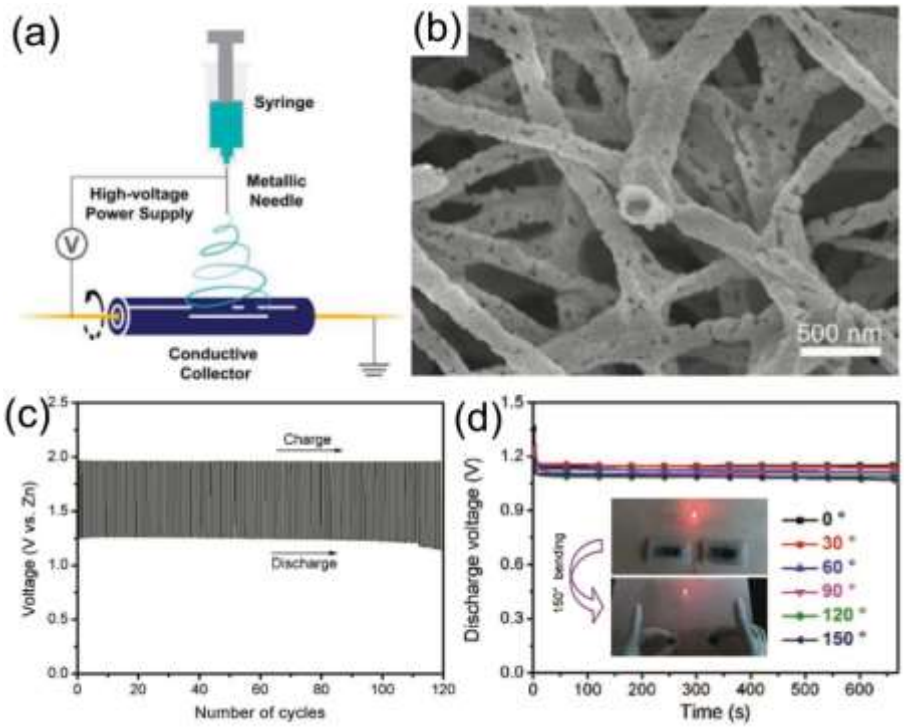

Figure 6 (a) Schematic diagram of typical electrospinning setup. Reproduced with permission from Ref. [12], © Wiley-VCH 2018. (b) Scanning electron micrograph of S-doped $CaMnO_3$ (CMO/S). (c) Galvanostatic pulse cycling of CMO/S at 5 mA cm^{-2}; cycle duration of 400 s. (d) Photographs of red light emitting diode powered by flexible Zn–air batteries at the bending angles of 0° and 150°. Reproduced with permission from Ref. [72], © Wiley-VCH 2018.

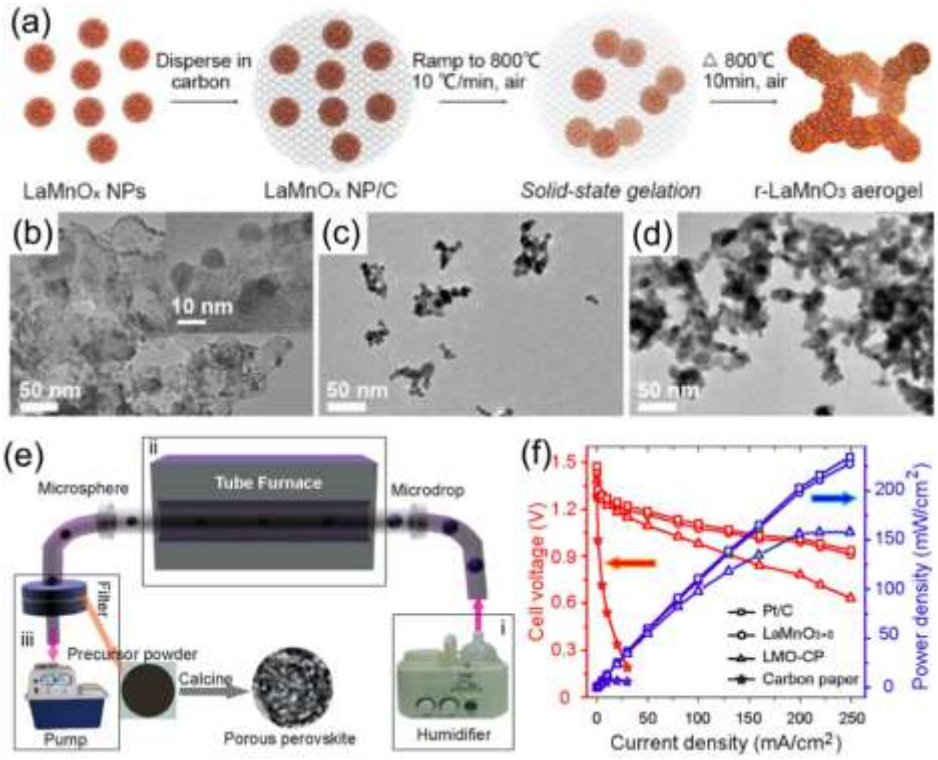

Figure 7 (a) Schematic illustration of solid-state gelation mechanism of transformation of "$LaMnO_x$" nanoparticles (NPs) to r-$LaMnO_{3\pm\delta}$ aerogel. Transmission electron micrographs of (b) "LaMnO*x*" NPs dispersed on porous carbon, (c) intermediate state during gelation, and (d) r-$LaMnO_{3\pm\delta}$ perovskite oxide aerogel. Reproduced with permission from Ref. [73], © American Chemical Society 2019. (e) Synthesis procedure of mesoporous $LaMnO_{3+\delta}$. (f) I–V and I–P plots of Zn–air batteries using bare, mesoporous $LaMnO_{3+\delta}$, $LaMnO_3$ NPs prepared via co-precipitation, and commercial Pt/C catalysts. Reproduced with permission from Ref. [74], © Elsevier 2018. Here I, V, and P denote the current density, cell voltage, and power density, respectively.

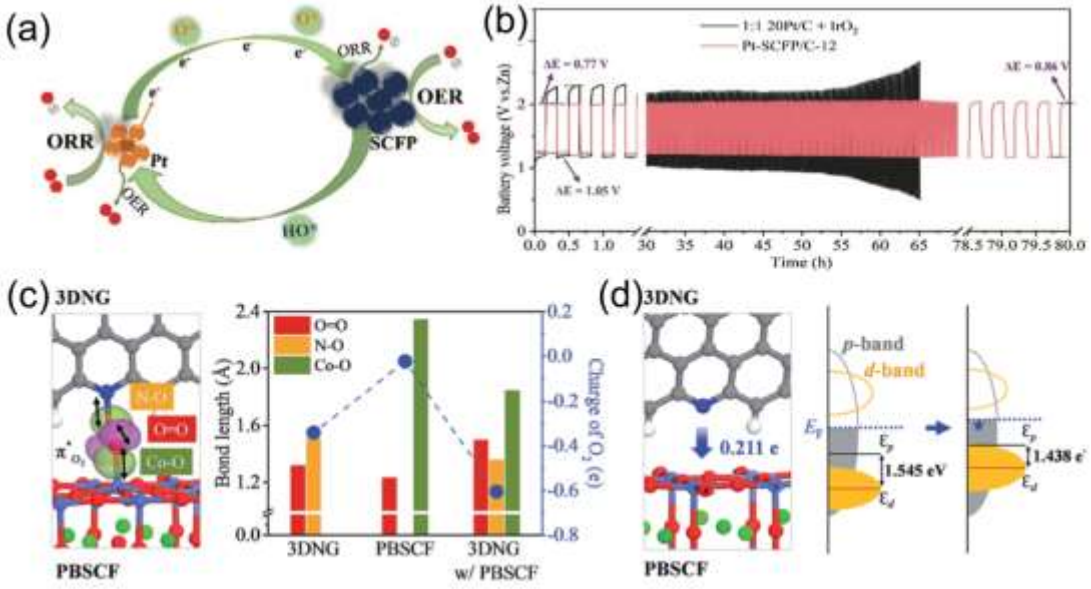

Figure 8 (a) Schematic illustrations of electronic interaction and spillover effect in Pt-SCFP/C-ab composites for the oxygen reduction and oxygen evolution reactions. (b) Galvanostatic charge–discharge profiles of Zn–air batteries incorporated with Pt-SCFP/C-12 or 1:1 20 wt% Pt/C + IrO_2 mixture catalysts at 5 mA cm^{-2}. Reproduced with permission from Ref. [78], © Wiley-VCH 2020. (c) Adsorption of O_2 on the surface of 3D N-doped graphene (3DNG) with $(PrBa_{0.5}Sr_{0.5})_{0.95}Co_{1.5}Fe_{0.5}O_{5+\delta}$ (PBSCF) (left), and lengths of O=O, N–O, and Co–O bonds, and charge of O_2 for O_2-adsorbed 3DNG, PBSCF, and 3DNG with PBSCF systems (right). (d) Charge transfer from 3DNG to PBSCF (left) and schematic band diagrams of PBSCF and PBSCF with 3DNG (right). Reproduced with permission from Ref. [70], © Royal Society of Chemistry 2019.

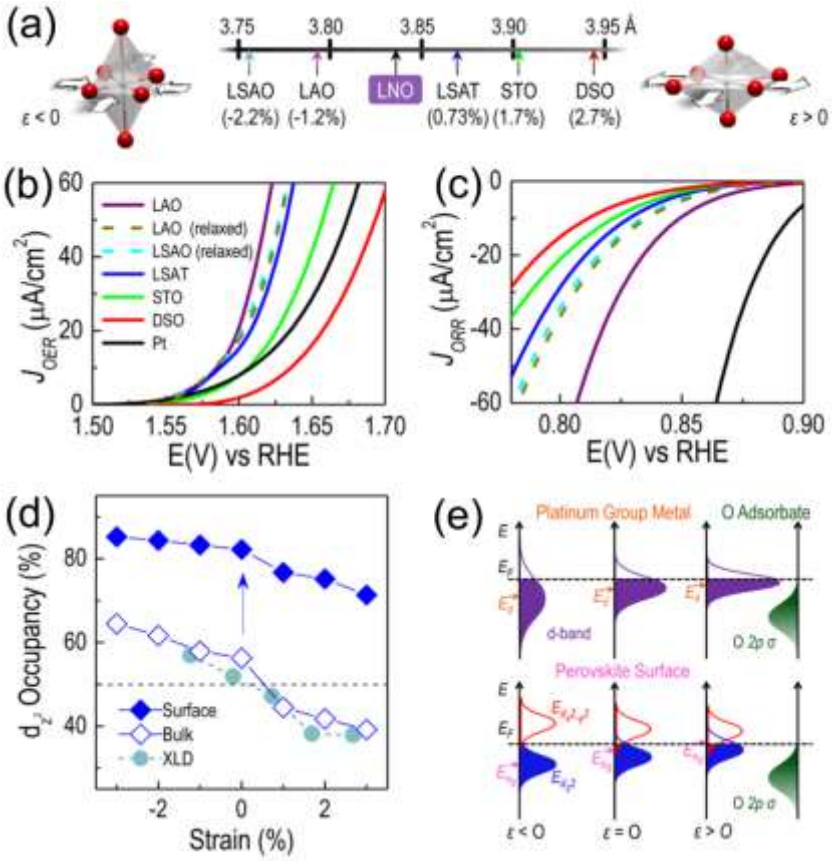

Figure 9 (a) Lattice parameters and associated strain for $LaNiO_3$ (LNO) deposited on different substrates. (b) Oxygen reduction reaction and (c) oxygen evolution reaction polarization curves of LNO films loaded on various substrates. (d) Orbital polarization results based on modeled data and experimental X-ray linear dichroism data. (e) Schematics associating this trend in perovskite oxides with the d-band center (Ed) of Pt. Reproduced with permission from Ref.[92], ⓒ American Chemical Society 2016.

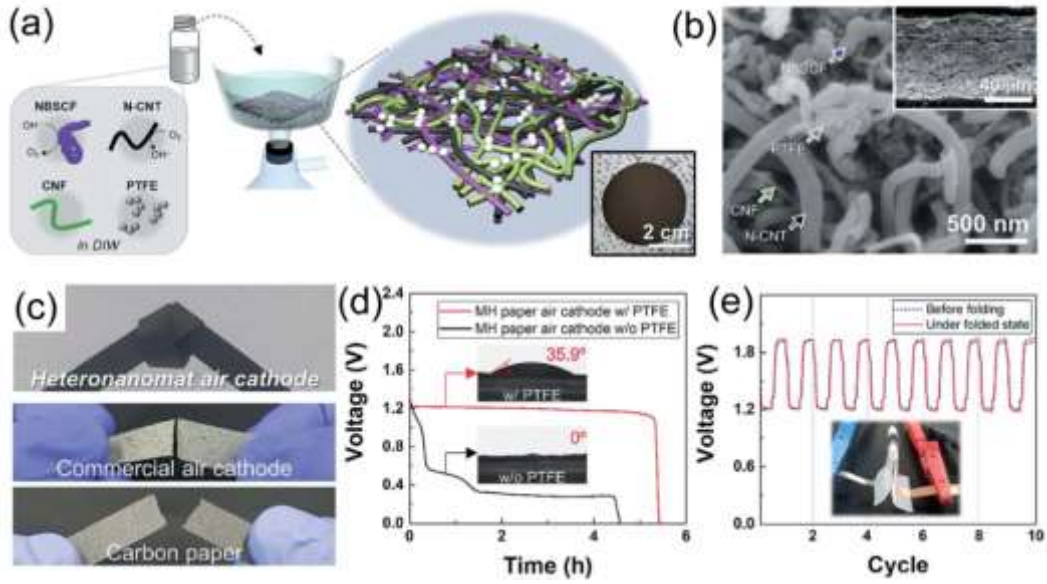

Figure 10 (a) Schematic of fabrication procedure of monolithic heteronanomat (MH) paper air cathode and its photograph. (b) Cross-sectional scanning electron micrograph of highly entangled network structure of the 1D cathode components. The inset depicts a low-magnification image. (c) Photographs illustrating the mechanical flexibility of MH paper air cathode and control samples (commercial air cathode and carbon paper). (d) Discharge profiles of MH paper air cathodes (with and without polytetrafluoroethylene nanoparticles). Insets present the water contact angles of the cathodes. (e) Galvanostatic discharge–charge cycle profiles before and after folding. Inset illustrates a photograph of the folded Zn–air battery. Reproduced with permission from Ref. [96], ⓒ Royal Society of Chemistry 2019.